



# A Multitransition Methanol Survey toward a Large Sample of High-mass Star-forming Regions

J. Y. Zhao<sup>1</sup>, J. S. Zhang<sup>1</sup> , Y. X. Wang<sup>1</sup> , J. J. Qiu<sup>2,3,4</sup> , Y. T. Yan<sup>5</sup> , H. Z. Yu<sup>6</sup> , J. L. Chen<sup>1</sup> , and Y. P. Zou<sup>1</sup> <sup>1</sup>Center for Astrophysics, Guangzhou University, Guangzhou, 510006, People's Republic of China; [jszhang@gzhu.edu.cn](mailto:jszhang@gzhu.edu.cn)<sup>2</sup>School of Physics and Astronomy, Sun Yat-sen University, Zhuhai 519082, People's Republic of China<sup>3</sup>CSST Science Center for the Guangdong-Hongkong-Macau Greater Bay Area, Sun Yat-Sen University, Zhuhai, People's Republic of China<sup>4</sup>Key Laboratory of Modern Astronomy and Astrophysics (Nanjing University), Ministry of Education, People's Republic of China<sup>5</sup>Max-Planck-Institut für Radioastronomie, Auf dem Hügel 69, D-53121 Bonn, Germany<sup>6</sup>Ural Federal University, 19 Mira Street, 620002 Ekaterinburg, Russia

Received 2022 November 12; revised 2023 February 27; accepted 2023 March 4; published 2023 June 2

## Abstract

We carried out a spectral line survey of CH<sub>3</sub>OH toward a large sample of 175 high-mass star-forming regions in the 3 mm, 2 mm, and 1.3 mm bands with the Institut de Radioastronomie Millimétrique (IRAM) 30 m telescope. Out of our 175 targets, 148 sources were detected with one or more CH<sub>3</sub>OH transition lines. Nineteen CH<sub>3</sub>OH transition lines, including 13 thermal lines and 6 maser lines, were detected. The 8<sub>0</sub> → 7<sub>1</sub> A<sup>+</sup> (~95.169 GHz) CH<sub>3</sub>OH maser line, one of the strongest class I CH<sub>3</sub>OH maser lines, was detected in 52 sources. Forty-two of them are previously reported masers and the other 10 are new detections. Through analyzing the rotational diagram of the detected CH<sub>3</sub>OH emission lines (nonmasing lines), we obtained the rotational temperature and the column density for 111 sources. Our results show that E-type CH<sub>3</sub>OH tends to have lower column density than A-type CH<sub>3</sub>OH. The column density ratio of E/A was derived in 55 sources with the majority having a ratio less than 1.0 (about 70%), with a peak ratio of ~0.6. This is consistent with theoretical predictions, i.e., overabundance of A-type CH<sub>3</sub>OH at low temperature leading to a low E/A ratio. Furthermore, we found that CH<sub>3</sub>OH abundance decreases beyond T<sub>dust</sub> ~ 30 K, which is supported by modeling results. All these support the fact that CH<sub>3</sub>OH is easily formed at low-temperature environments, via successive hydrogenation of CO on cold dust surfaces.

*Unified Astronomy Thesaurus concepts:* [Interstellar molecules \(849\)](#); [Astrochemistry \(75\)](#); [Molecule formation \(2076\)](#)

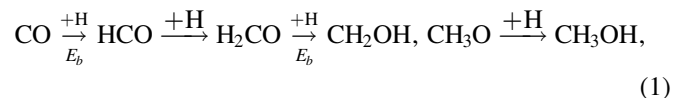
*Supporting material:* figure sets, machine-readable tables

## 1. Introduction

More than 270 molecules<sup>7</sup> have been detected in the interstellar medium (ISM). Molecules with six or more atoms are called complex molecules, and those molecules among them that contain carbon are called organic molecules. In the ISM, complex organic molecules are only detected in sources of relatively high density. Based on their spectral and chemical properties, complex molecules are excellent probes of the physical conditions and evolution of the regions where they are located (Herbst & van Dishoeck 2009).

Methanol (CH<sub>3</sub>OH), a complex organic molecule, is known as a good tracer of the physical conditions in high-mass star-forming regions (HMSFRs) (Mangum & Wootten 1993; Leurini et al. 2004; Herbst & van Dishoeck 2009; Guzmán et al. 2013; Mangum et al. 2013). Due to the internal rotation of the OH group, the transition lines of CH<sub>3</sub>OH are abundant at the millimeter and submillimeter bands and some of them are close enough to be observed simultaneously with a limited frequency coverage (Leurini et al. 2004; Levshakov et al. 2011). Meanwhile, because CH<sub>3</sub>OH is an asymmetric top molecule, it can be used to analyze the high-density environment (Menten et al. 1988) and is sensitive to kinetic

temperature (Leurini et al. 2004). Moreover, CH<sub>3</sub>OH is ubiquitous and widely associated with interstellar environments (Leurini et al. 2004; Guzmán et al. 2013). Given its chemical formation, it is now assumed that CH<sub>3</sub>OH in the ISM is a result of the hydrogenation of carbon monoxide (CO) molecules formed on the surface of dust particles. Then CH<sub>3</sub>OH is desorbed to the gas phase by thermal and nonthermal processes (Watanabe & Kouchi 2002; Fuchs et al. 2009; Linnartz et al. 2015). The following is the process of conventional hydrogenation from CO to CH<sub>3</sub>OH (Watanabe & Kouchi 2002) that occurs on ices:



where  $E_b$  is the activation energy barrier.

Detectable CH<sub>3</sub>OH emissions are included in both maser and thermal lines. Recently, a wealth of maser observations (e.g., Yang et al. 2017, 2020; Yang et al. 2017, 2019; Song et al. 2022) and maser surveys (e.g., the Methanol Multi-beam Survey; Breen et al. 2012a, 2012b, 2014, 2016, 2018; Cunningham et al. 2018) have been conducted. Similarly, many observational studies have been carried out for CH<sub>3</sub>OH thermal lines. Some studies have investigated the properties of CH<sub>3</sub>OH in specific sources, e.g., Orion-KL (Menten et al. 1986, 1988), Orion A (Sutton et al. 1985; Blake et al. 1986), Sgr B2 and Sgr A (Ball et al. 1970), and OMC-1 (Blake et al. 1987). There have also been some studies of small samples for CH<sub>3</sub>OH thermal lines. Hatchell et al. (1998) carried out a line survey in

<sup>7</sup> <https://cdms.astro.uni-koeln.de/classic/molecules>

14 ultracompact H II regions and detected four CH<sub>3</sub>OH thermal lines. Both Minier & Booth (2002) and Sun et al. (2012) detected four CH<sub>3</sub>OH thermal lines, through a line survey toward a sample of 23 and 13 HMSFRs, respectively. Leurini (2005) performed CH<sub>3</sub>OH observations toward 13 sources consisting of infrared-dark clouds and high-mass protostellar objects and detected six thermal lines. Four CH<sub>3</sub>OH thermal lines were detected in a targeted 3 mm spectral line survey toward a sample of 83 star-forming clumps with a CH<sub>3</sub>OH maser (Purcell et al. 2009). He et al. (2012) detected 15 CH<sub>3</sub>OH thermal lines toward one sample of Spitzer Galactic Legacy Infrared Mid-plane Survey Extraordinaire extended green objects. A survey of molecular lines was undertaken by Chen et al. (2013) in the 3 mm band toward 57 young stellar objects and five CH<sub>3</sub>OH thermal lines were detected. These studies on CH<sub>3</sub>OH thermal lines mostly focused on individual cases or small samples. Here we present one multiple-transition CH<sub>3</sub>OH survey toward a large sample of 175 HMSFRs, through the most sensitive millimeter telescope, the Institut de Radioastronomie Millimétrique (IRAM) 30 m telescope<sup>8</sup> at the Pico Veleta Observatory (Granada, Spain). Our sample was mainly taken from the Bar and Spiral Structure Legacy (BeSSeL) project (Reid et al. 2014, 2019) sample, which provides accurate distance values by measurements of trigonometric parallaxes and proper motions for masers (131 out of 175). Forty-four star formation regions associated with IRAS sources with relatively strong CO emission (the corrected antenna temperature of  $T_A^* > 10$  K from Wouterloot & Brand 1989) were also chosen.

The observations are described in Section 2. Our analyses of the measured spectral lines and the corresponding results are presented in Section 3. In Section 4, we analyze the ratio between A- and E-type CH<sub>3</sub>OH abundances, and discuss the relationships between CH<sub>3</sub>OH abundance and other evolutionary indicators of HMSFRs. A summary is presented in Section 5.

## 2. Observation

The observations were performed in 2016 June, 2020 August and September, and 2021 April toward our sample with the IRAM 30 m telescope. The Eight Mixer Receiver (EMIR) with dual polarization and the Fourier transform spectrometer backend were used to cover the frequency ranges of 90.6–98.2 GHz in the 3 mm band, 108.0–115.4 GHz and 138.4–146.0 GHz in the 2 mm band, and 215.6–224.2 GHz in the 1.3 mm band. The standard position switching mode was carried out with the off position at a (−30′, 0′) or (30′, 0′) offset in R.A. and decl., or in the azimuth from the source. The main-beam brightness temperature ( $T_{\text{mb}}$ ) was calculated from the antenna temperature ( $T_A^*$ ) with the expression  $T_{\text{mb}} = T_A^* \frac{F_{\text{eff}}}{B_{\text{eff}}}$ , where  $F_{\text{eff}}$  and  $B_{\text{eff}}$  are the forward efficiency and main-beam efficiency of the IRAM 30 m telescope. All parameters related to the observations including the beam size,  $F_{\text{eff}}$ ,  $B_{\text{eff}}$ , velocity resolution, rms level, typical system temperature, and observation date at the corresponding bands are summarized in Table 1.

<sup>8</sup> IRAM is supported by Institut National des Sciences de l’Univers/Centre National de la Recherche Scientifique (INSU/CNRS, France), Max-Planck-Gesellschaft (Germany), and Instituto Geográfico Nacional (Spain).

## 3. Results and Analysis

### 3.1. Spectral Fitting Results

The molecule lines were identified using information from the Cologne Database for Molecular Spectroscopy catalog<sup>9</sup> (CDMS; Müller et al. 2001, 2005), the Jet Propulsion Laboratory database<sup>10</sup> (JPL; Pickett et al. 1998), and the Splatalogue database for astronomical spectroscopy.<sup>11</sup> Data reduction was conducted with the Continuum Line Analysis Signal-dish Software (CLASS) of the Grenoble Image and Line Data Analysis Software packages (GILDAS; e.g., Guilloteau & Lucas 2000).<sup>12</sup> All detected lines were processed by subtracting baselines. In order to maintain consistent velocity resolution (0.4–0.6 km s<sup>−1</sup>), the spectra in the band of 215.6–224.2 GHz with different resolution were smoothed. Those sources with narrow spectral profiles around the maser transitions of 216.945 GHz and 218.440 GHz were not smoothed, to avoid smoothing potential maser lines. We used Gaussian fits for detected lines with signal-to-noise ratios  $\geq 3$ . Figure 1 displays the spectra with fit lines for each source. Information on the detected CH<sub>3</sub>OH lines is listed in Table 2 and information on the targeted sources is listed in Table 3. The spectral fitting parameters of each source, including the integrated line intensity, local standard of rest (LSR) velocity ( $V_{\text{LSR}}$ ), FWHM, and main brightness temperature ( $T_{\text{mb}}$ ), are shown in Table 4. We successfully detected 19 CH<sub>3</sub>OH transitions in total. Out of our 175 targets, 148 sources were detected with one or more CH<sub>3</sub>OH transitions. The most abundant detections consisting of 19 lines were made toward one source (G109.87+02.11) and only one transition was detected in WB89 163. The source numbers for detections of each transition are summarized in column (6) of Table 2, and the numbers of detected lines for each source are summarized in column (6) of Table 3.

Apart from the 95 GHz CH<sub>3</sub>OH maser (see details in the following subsection, Section 3.2), five known CH<sub>3</sub>OH maser lines were covered in our observations:  $8_3 \rightarrow 9_2$  E at 94 GHz,  $0_0 \rightarrow 1_{-1}$  E at 108 GHz,  $7_2 \rightarrow 8_1$  A<sup>+</sup> at 111 GHz,  $5_1 \rightarrow 4_2$  E at 216 GHz, and  $4_2 \rightarrow 3_1$  E at 218 GHz (Nakano & Yoshida 1986; Sobolev et al. 1997; Cragg et al. 2005; Hunter et al. 2014; Leurini et al. 2016). We checked these maser transitions in our spectra and found narrow maser features in 12 sources. Those tentative maser features were normally overlaid on a broad-line profile (see Figure 1). The line parameters for both maser and thermal components for these 12 sources are listed in Table 5.

### 3.2. 95 GHz CH<sub>3</sub>OH Maser Detection

More than 70 CH<sub>3</sub>OH maser transitions have been detected to date, and in particular more than 30 transitions have been detected toward maser flare source G358.93−0.03 (Cragg et al. 2005; Breen et al. 2019; Brogan et al. 2019; Chen et al. 2019; Miao et al. 2022). CH<sub>3</sub>OH maser transitions are empirically classified into two categories, class I and class II (Batra et al. 1987; Menten 1991). Class II CH<sub>3</sub>OH masers are known to be radiatively pumped (Cragg et al. 2005) and detected in regions close to high-mass protostars (within 1′′) (Ellingsen 2006; Caswell et al. 2010). Class I CH<sub>3</sub>OH masers are produced by collisional pumping (Cragg et al. 1992; Leurini et al. 2016) and

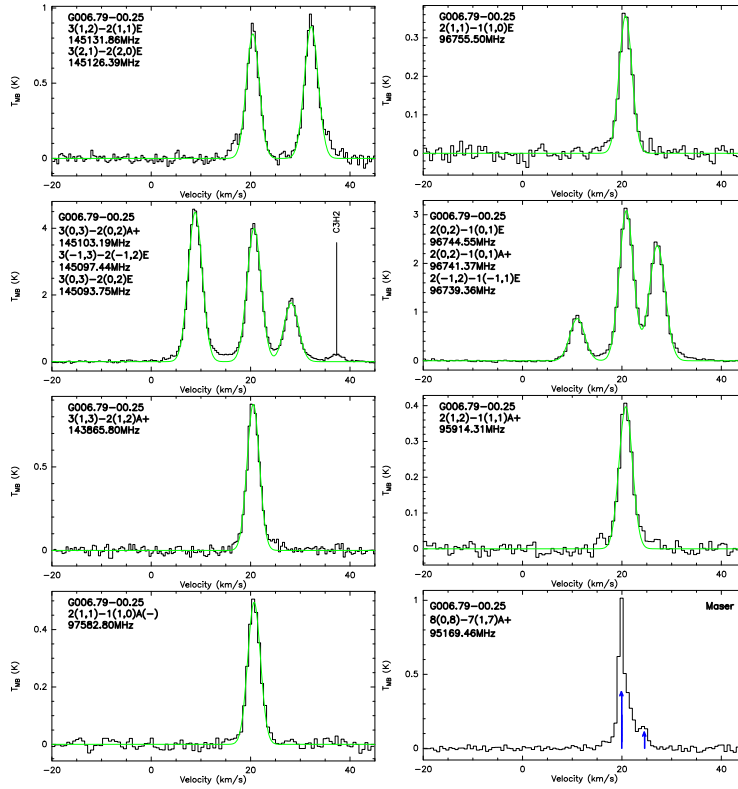
<sup>9</sup> <https://cdms.astro.uni-koeln.de>

<sup>10</sup> <https://spec.jpl.nasa.gov/ftp/pub/catalog/catform.html>

<sup>11</sup> <https://splatalogue.online//advanced.php>

<sup>12</sup> <http://www.iram.fr/IRAMFR/GILDAS>

G006.79-00.25



G023.20-00.37

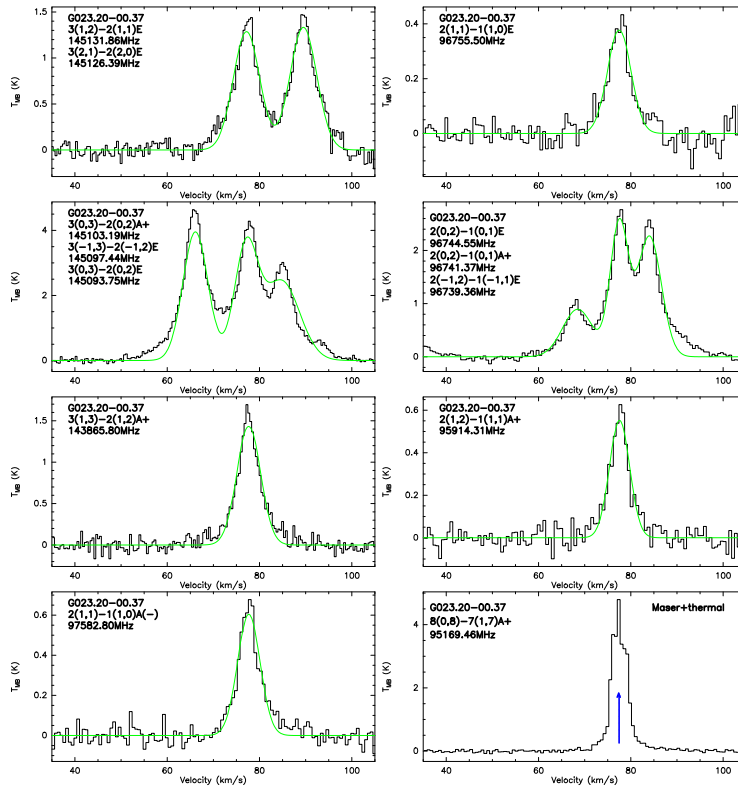


**Figure 1.** The IRAM 30 m spectra of the  $\text{CH}_3\text{OH}$  multitransitions with green fit lines of our 148 sources. Those without fit lines are due to the blending of transition lines in their spectra or to narrow features. For those narrow tentative maser features, we mark them with blue arrows and corresponding text of “maser” in the upper right corner. For those with narrow tentative maser features overlaid on a broad thermal line profile, we mark them with blue arrows and text of “maser+thermal” in the upper right corner.

(The complete figure set (148 images) is available.)

**Table 1**  
Summary of Observation Information

Band Range (GHz)	Beam Size ( $''$ )	$F_{\text{eff}}$	$B_{\text{eff}}$	$\delta V$ ( $\text{km s}^{-1}$ )	rms Range (K)	System Temperatures (K)	Date
(1)	(2)	(3)	(4)	(5)	(6)	(7)	(8)
215.6–224.2	10	0.96	0.63	0.3	0.01–0.26	350–1000	2020 Sep, 2021 Apr
138.4–146.0	14	0.93	0.73	0.4	0.01–0.21	150–250	2020 Aug
108.0–115.4	18	0.94	0.78	0.6	0.01–0.17	150–250	2016 Jun, 2020 Sep, 2021 Apr
90.6–98.2	25	0.95	0.81	0.5	0.01–0.51	90–260	2016 Jun, 2020 Aug

**Note.** Taken from the IRAM website.

**Table 2**  
Information on Targeted Transition Lines of CH<sub>3</sub>OH

Transition (1)	Frequency (MHz) (2)	$E_u/k$ (K) (3)	$S\mu^2$ ( $\text{D}^2$ ) (4)	Maser or Thermal (5)	Number of Sources (6)
8 <sub>3,5</sub> – 9 <sub>2,7</sub> E	94,541.7850	123.39	2.23	M&T	10
8 <sub>0,8</sub> – 7 <sub>1,7</sub> A+	95,169.4630	83.54	7.22	M&T	69
2 <sub>1,2</sub> – 1 <sub>1,1</sub> A+	95,914.3100	21.44	1.21	T	46
2 <sub>-1,2</sub> – 1 <sub>-1,1</sub> E	96,739.4630	4.65	1.21	T	114
2 <sub>0,2</sub> – 1 <sub>0,1</sub> A+	96,741.3710	6.97	1.62	T	116
2 <sub>0,2</sub> – 1 <sub>0,1</sub> E	96,744.5450	12.20	1.62	T	82
2 <sub>1,1</sub> – 1 <sub>1,0</sub> E	96,755.5010	20.13	1.24	T	41
2 <sub>1,1</sub> – 1 <sub>1,0</sub> A–	97,582.7980	21.56	1.21	T	50
0 <sub>0,0</sub> – 1 <sub>-1,1</sub> E	108,893.9450	5.23	0.98	M&T	58
7 <sub>2,5</sub> – 8 <sub>1,8</sub> A+	111,289.4530	102.72	2.43	M&T	20
3 <sub>1,3</sub> – 2 <sub>1,2</sub> A+	143,865.7950	28.35	2.16	T	48
3 <sub>0,3</sub> – 2 <sub>0,2</sub> E	145,093.7540	19.16	2.42	T	72
3 <sub>-1,3</sub> – 2 <sub>-1,2</sub> E	145,097.4350	11.62	2.16	T	84
3 <sub>0,3</sub> – 2 <sub>0,2</sub> A+	145,103.1850	13.93	2.43	T	84
3 <sub>2,1</sub> – 2 <sub>2,0</sub> E	145,126.3860	31.94	1.35	T	42
3 <sub>1,2</sub> – 2 <sub>1,1</sub> E	145,131.8640	27.09	2.20	T	41
5 <sub>1,4</sub> – 4 <sub>2,2</sub> E	216,945.5210	47.98	1.23	M&T	28
4 <sub>2,2</sub> – 3 <sub>1,2</sub> E	218,440.0630	37.57	3.38	M&T	44
8 <sub>0,8</sub> – 7 <sub>1,6</sub> E	220,078.5610	88.72	3.45	T	26

**Note.** Columns (1)–(2): transition of CH<sub>3</sub>OH and corresponding frequency. Column (3): energy of upper level relative to the  $J_K = 0_0$  level of A-type CH<sub>3</sub>OH and relative to  $J_K = 1_{-1}$  level for E-type CH<sub>3</sub>OH. Column (4): product of the total torsion-rotational line strength and the square of the electric dipole moment for each transition. The values of  $E_u/k$  and  $S\mu^2$  were taken from CDMS, JPL, and Splatalogue. Column (5): M for maser line and T for thermal emission line. Column (6): the source number for detection of each transition.

commonly distributed on a larger spatial scale (0.1–1 pc) around the exciting source (Kurtz et al. 2004; Cyganowski et al. 2009; McCarthy et al. 2018). They can be used to trace mild shocks related to molecular clouds driven by high- or low-mass protostar outflows, expanding H II regions (Voronkov et al. 2010; Chen et al. 2011, 2022), or supernova remnants (Pihlström et al. 2011, 2014).

We made a detailed analysis of the 95 GHz emission line in our sample. Following the commonly used method (Chen et al. 2013; Yang et al. 2017), we identified the 95 GHz CH<sub>3</sub>OH emission in 69 sources. The criterion for identifying the maser is related to the line width of the spectral line. The line width of the maser feature is expected to be narrower than that of the thermal lines. In particular, all detected class I CH<sub>3</sub>OH masers show one or more narrow spectral features, and the typical line width is 1 km s<sup>-1</sup> (Chen et al. 2013). Eighty-five percent of class I CH<sub>3</sub>OH masers have a line width narrower than

2.5 km s<sup>-1</sup> (Yang et al. 2017). Thus a line width of less than 2.5 km s<sup>-1</sup> was taken for our 95 GHz CH<sub>3</sub>OH maser. According to the source coordinates, we crossmatched our sample with the maser database compiled by Ladeyschikov et al. (2019), using a radius of 25 $''$  (the biggest beam size in our observations). Among the 69 sources with 95 GHz CH<sub>3</sub>OH emission, 42 sources have been reported to be maser sources (Yang et al. 2017; Ladeyschikov et al. 2019). For the remaining 27 sources, 10 meet the criterion, i.e., the line widths of 95 GHz emissions in the 10 sources are smaller than 2.5 km s<sup>-1</sup>. The 10 sources are considered to be newly detected in maser (see Figure 2). For the other 17 sources, the spectral line widths are much larger than 2.5 km s<sup>-1</sup> and they cannot be classified as maser sources. The peak flux density of the 10 newly detected 95 GHz CH<sub>3</sub>OH masers ranges from 0.81 to 4.32 Jy and their integrated intensities range from 1.04 to 8.22 Jy km s<sup>-1</sup>. Thus the corresponding isotropic maser luminosity of these sources can be obtained, using  $L_m = 4\pi D^2 S_{\text{int}} \lambda^{-1}$  (Chen et al. 2013), where  $D$  is the kinematic distance, measured by a maser parallax method (Reid et al. 2014, 2019);  $S_{\text{int}}$  is the integrated flux density; and  $\lambda$  is the wavelength of the 95 GHz CH<sub>3</sub>OH maser (see details in Table 6).

### 3.3. Line Width of CH<sub>3</sub>OH Nonmasing Lines

#### 3.3.1. Line Width of Different Transitions

The line information related to the state of turbulence and the region where the gas is mainly emitting can be inferred from the line width of the Gaussian fitted to the observed profiles (Beuther et al. 2002). The line width consists of thermal and nonthermal components. The thermal and nonthermal line width can be calculated by  $\sigma_T = \sqrt{\frac{kT}{m}}$  and  $\sigma_{\text{NT}} = \sqrt{\frac{\Delta v^2}{8 \ln 2} - \sigma_T^2}$ , respectively (Tang et al. 2018), where  $k$  is the Boltzmann constant, and  $m = 32$  amu is the molecular mass for CH<sub>3</sub>OH. Using a mean unweighted kinetic temperature of  $\sim 30$  K (the mean value of our sample; see Section 3.4) and the average line width of CH<sub>3</sub>OH ( $\sim 4.66$  km s<sup>-1</sup>) for our sample, the line width accounted for by the thermal and nonthermal components is 0.09 and 1.98 km s<sup>-1</sup>, respectively. The thermal line width is much smaller than the nonthermal line width. The sound speed ( $a_s = \sqrt{\frac{kT_{\text{kin}}}{\mu m_{\text{H}}}}$ , where  $\mu = 2.37$  is the mean molecular weight for molecular clouds and  $m_{\text{H}}$  is the mass of the hydrogen atom) is 0.32 km s<sup>-1</sup> at temperature 30 K. Consequently, the Mach number  $M = \frac{\sigma_{\text{NT}}}{a_s}$  is 4.31 for our sample, which agrees with previous results (the mean value 4.2 derived from H<sub>2</sub>CO; Tang et al. 2018). This suggests that our sources are turbulently dominated and the line width of CH<sub>3</sub>OH is strongly influenced by supersonic nonthermal motion.

**Table 3**  
Information on Detected CH<sub>3</sub>OH Transition Lines

Source Name	R.A.	Decl.	The ATLASGAL Catalog Source Name	$D_{GC}$	Number of Methanol Lines	Maser Detection
(1)	J2000 (2)	J2000 (3)	(4)	(kpc) (5)	(6)	(7)
WB89 380	01:07:50.70	+65:21:21.40	...	17.02	2	...
WB89 391	01:19:26.50	+65:45:44.82	...	16.91	2	...
G133.94+01.06	02:27:03.81	+61:52:25.23	...	9.58	12	95.169 GHz, 111.289 GHz
WB89 434	02:41:29.40	+60:43:14.70	...	16.24	0	...
G135.27+02.79	02:43:28.56	+62:57:08.38	...	13.08	5	111.289 GHz
WB89 437	02:43:30.30	+62:57:11.60	...	16.24	5	108.893 GHz
WB89 440	02:46:08.07	+62:46:08.70	...	16.44	0	...
WB89 477	03:17:30.60	+60:32:08.40	...	13.46	0	...
WB89 501	03:52:29.10	+57:48:32.30	...	16.39	3	...

**Note.** Column (1): source name. Columns (2) and (3): targeted position (R.A. and decl. coordinates) for our sample. Column (4): name of associated source in Urquhart et al. (2018). Column (5): the galactocentric distance  $D_{GC}$ . Column (6): the number of methanol lines detected in each source. Column (7): ellipses stand for no maser detected. The transition in the column indicates that a maser was detected on this transition.

(This table is available in its entirety in machine-readable form.)

**Table 4**  
Measured CH<sub>3</sub>OH Spectral Line Parameters toward Our Sample by the IRAM 30 m Telescope

Source Name	Freq. (MHz)	rms (K)	$\int T_{mb} dv$ (K km s <sup>-1</sup> )	$V_{LSR}$ (km s <sup>-1</sup> )	$\Delta V$ (km s <sup>-1</sup> )	$T_{mb}$ (K)
(1)	(2)	(3)	(4)	(5)	(6)	(7)
WB89 380	96,741.37	0.01	0.21 (0.02)	-86.44 (0.16)	3.49 (0.40)	0.05
	96,739.36	0.01	0.09 (0.02)	-80.08 (0.20)	2.34 (0.45)	0.03
WB89 391	96,741.37	0.01	0.12 (0.01)	-86.03 (0.08)	1.46 (0.20)	0.07
	96,739.36	0.01	0.05 (0.01)	-79.79 (0.10)	0.87 (0.39)	0.04
G133.94+01.06	220,078.56	0.03	10.83 (0.18)	-45.80 (0.04)	4.99 (0.10)	1.39
	218,440.06	0.02	25.17 (0.06)	-46.06 (0.01)	4.52 (0.01)	3.56

**Note.** Sources with blank values are those with nondetections or those that could not be given a reliable fit due to blending features narrow maser features in the spectra. Those with frequency in bold style are newly detected CH<sub>3</sub>OH masers. Column (1): source name. Column (2): frequency of transition lines. Column (3): the rms value of  $T_{mb}$ . Column (4): the integrated line intensity, with its error in parentheses. Column (5): LSR velocity. Column (6): FWHM. Column (7): peak  $T_{mb}$  value.

(This table is available in its entirety in machine-readable form.)

**Table 5**  
Line Parameters of Sources with Spectra of Tentative Maser Component Overlaid on Broad Thermal Component

Freq. (MHz)	Source Name (2)	Quasi-thermal				Tentative Maser Components		
		$V_c$ (km s <sup>-1</sup> ) (3)	$T_p$ (K) (4)	$\Delta V$ (km s <sup>-1</sup> ) (5)	$W$ (K km s <sup>-1</sup> ) (6)	$V_c$ (km s <sup>-1</sup> ) (7)	$T_p$ (K) (8)	$V_r$ (km s <sup>-1</sup> ) (9)
218,440.06	G007.47+00.05	...	...	...	...	-15.43	0.17	-16.58, -14.73
						-13.89	0.17	-14.52, -13.29
216,945.52	G081.75+00.59	-3.99 (0.07)	0.26	2.10 (0.27)	0.58 (0.05)	-4.11	0.33	-4.38, -3.84
	G209.00-19.38	7.67 (0.10)	0.14	3.30 (0.24)	0.48 (0.03)	6.51	0.13	6.16, 7.12
111,289.45	G078.12+03.63	...	...	...	...	-7.71	0.15	-9.42, -6.16
						-3.94	0.10	-5.82, -3.08
						0.00	0.10	-3.94, -2.23
	G133.94+01.06	-45.98 (0.04)	0.66	5.77 (0.10)	3.44 (0.05)	-44.32	0.48	-44.74, -43.72
	G135.27+02.79	-72.40 (0.36)	0.02	7.04 (0.91)	0.15 (0.02)	-70.82	0.02	-72.06, -69.80
	G209.00-19.38	7.52 (0.08)	0.10	3.14 (0.22)	0.35 (0.02)	7.33	0.12	6.99, 7.88
108,893.95	WB89 437	-71.59 (0.17)	0.09	3.14 (0.48)	0.29 (0.03)	-71.64	0.10	-72.33, -70.55
	W33	36.02 (0.06)	0.54	5.39 (0.14)	3.11 (0.07)	34.93	0.57	33.90, 35.55
						36.99	0.54	36.37, 37.50
	G033.64-00.22	61.35 (0.23)	0.12	3.92 (0.53)	0.51 (0.06)	61.94	0.15	61.32, 62.40
	G105.41+09.87	-10.46 (0.21)	0.05	5.81 (0.53)	0.33 (0.02)	-10.23	0.07	-11.27, -9.29
94,541.79	G037.42+11.51	44.11 (0.20)	0.06	6.38 (0.47)	0.40 (0.03)	46.63	0.05	45.77, 47.57

**Note.** Column (1): the CH<sub>3</sub>OH maser transitions. Column (2): source name. Columns (3)–(6): the velocity at the peak  $V_c$ , the peak main-beam temperature  $T_p$ , the FWHM line width  $\Delta V$ , and the integrated intensity  $W$  of the main component. Columns (7)–(9): the line centroid  $V_c$ , the peak main-beam temperature  $T_p$ , and the velocity range of the narrow lines.

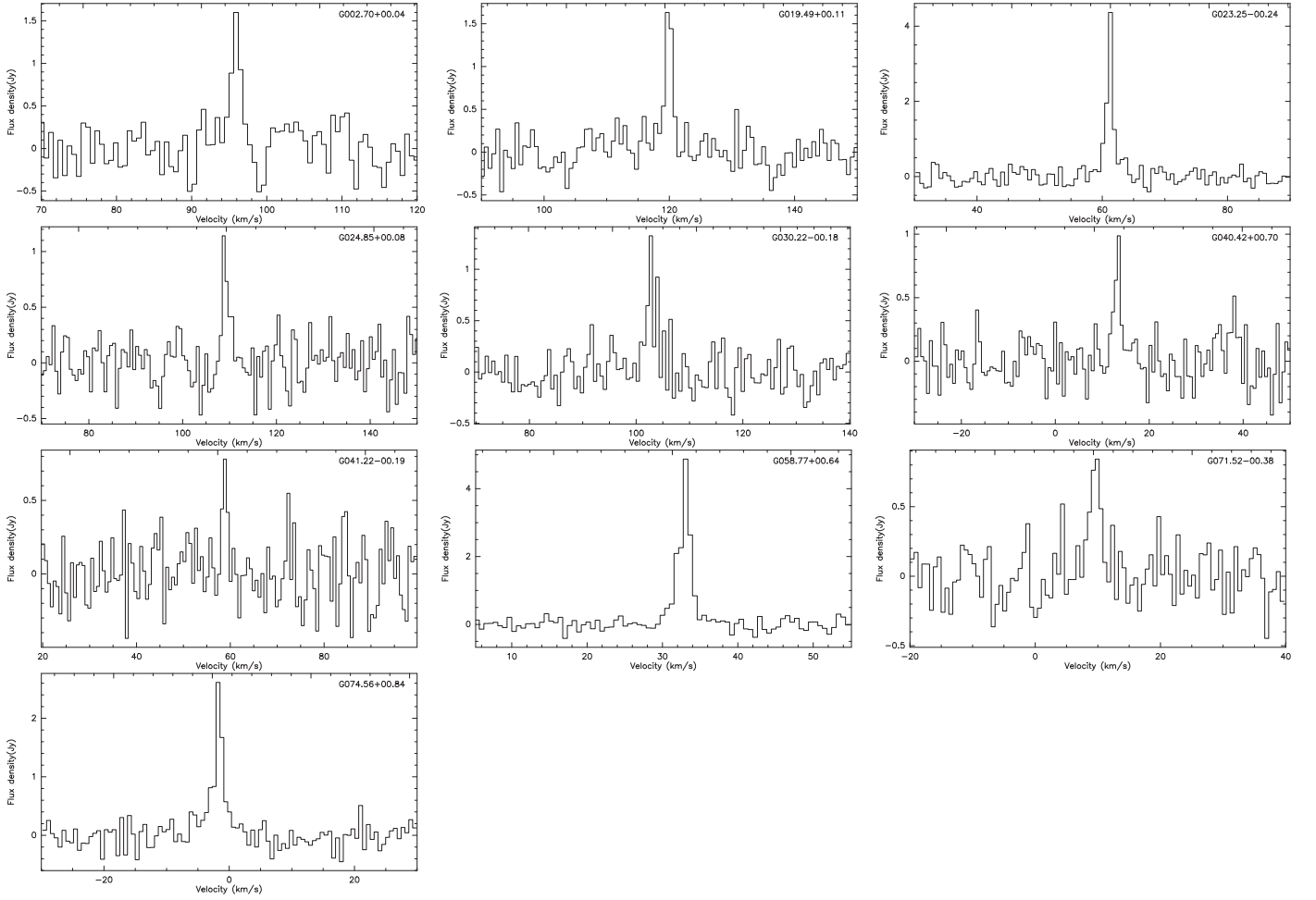


**Figure 2.** The spectra of the newly detected 95 GHz CH<sub>3</sub>OH masers from our survey.

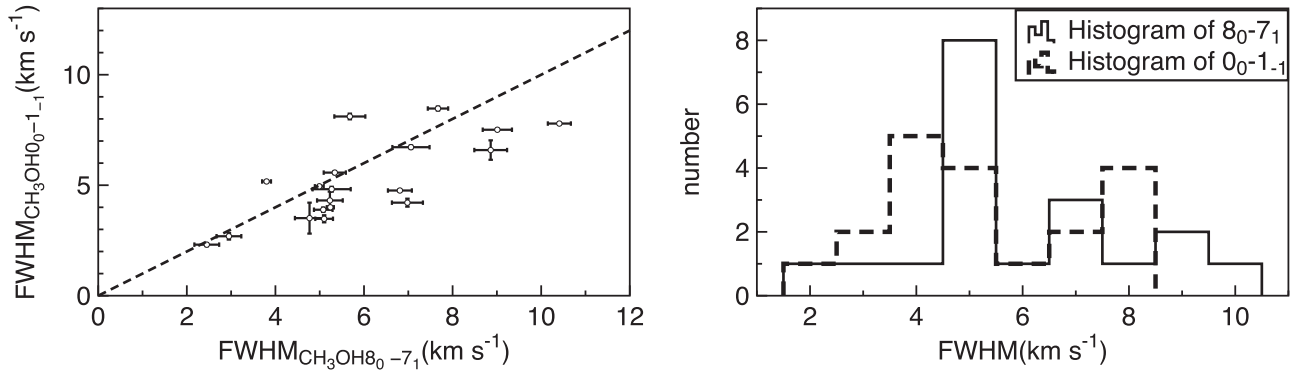


**Figure 3.** Left panel: Line width of CH<sub>3</sub>OH 0<sub>0,0</sub> → 1<sub>-1,1</sub> vs. line width of CH<sub>3</sub>OH 8<sub>0,8</sub> → 7<sub>1,7</sub> line. The dashed line indicates both lines have equal values of line width. Right panel: Histograms of the line widths for CH<sub>3</sub>OH 8<sub>0,8</sub> → 7<sub>1,7</sub> (solid lines) and CH<sub>3</sub>OH 0<sub>0,0</sub> → 1<sub>-1,1</sub> (dashed lines).

The line width of CH<sub>3</sub>OH nonmasing emission lines in our sample ranges from 0.70 to 22.53 km s<sup>-1</sup>. We compared the line widths of different transition lines of our sources and found that the line widths of higher-*J* transitions tend to be larger than those of lower-*J* transitions. To show this difference more clearly, two transitions with a large *J* difference were chosen for comparison, i.e., *J* = 8<sub>0,8</sub> → 7<sub>1,6</sub> E and 0<sub>0,0</sub> → 1<sub>-1,1</sub> E. We found that 19 sources were detected with both transition lines (*J* = 8 → 7 and 0 → 1). The line width of CH<sub>3</sub>OH *J* = 8 → 7 is

plotted against that of *J* = 0 → 1 for those 19 sources in Figure 3 (left panel), which shows an apparently larger line width for the *J* = 8 → 7 line (14 out of 19 sources). The mean line widths are  $5.93 \pm 0.27$  and  $5.20 \pm 0.16$  km s<sup>-1</sup> for the CH<sub>3</sub>OH 8 → 7 and 0 → 1 lines, respectively. The right panel of Figure 3 shows the distribution of line widths for the CH<sub>3</sub>OH 8 → 7 and 0 → 1 lines, where the peak of the *J* = 8 → 7 line is about 5 km s<sup>-1</sup> and the peak of the *J* = 0 → 1 line is about 4 km s<sup>-1</sup>. The results also support the observation that the line

**Table 6**  
Line Parameters of 95 GHz CH<sub>3</sub>OH Masers

Source Name	$S_p$ (Jy)	$V_p$ (km s <sup>-1</sup> )	$\Delta V$ (km s <sup>-1</sup> )	$S_{\text{int}}$ (Jy km s <sup>-1</sup> )	Distance (kpc)	$L$ (10 <sup>-6</sup> $L_{\odot}$ )
(1)	(2)	(3)	(4)	(5)	(6)	(7)
<b>G002.70+00.04</b>	1.54	95.9	94.7, 97.1	2.63 (0.39)	9.90	25.35 (3.72)
<b>G019.49+00.11</b>	1.77	120.0	118.7, 121.0	2.54 (0.27)	3.06	2.36 (0.25)
<b>G023.25-00.24</b>	4.32	61.1	60.1, 61.9	4.94 (0.24)	5.91	16.97 (0.82)
<b>G024.85+00.08</b>	1.02	108.2	108.2, 110.4	1.73 (0.35)	5.68	5.48 (1.10)
<b>G030.22-00.18</b>	0.92	103.0	101.6, 103.6	2.40 (0.35)	3.52	2.92 (0.42)
<b>G040.42+00.70</b>	0.89	13.3	11.8, 14.1	1.55 (0.28)	12.82	25.07 (4.59)
<b>G041.22-00.19</b>	0.81	58.8	57.8, 60.2	1.04 (0.25)	8.85	8.03 (1.89)
<b>G058.77+00.64</b>	4.14	32.9	32.4, 34.1	8.22 (0.29)	3.34	9.01 (0.32)
<b>G071.52-00.38</b>	0.85	9.6	8.2, 10.7	1.84 (0.31)	3.61	2.36 (0.40)
<b>G074.56+00.84</b>	2.34	-1.9	-2.6, -0.6	4.03 (0.38)	2.72	2.93 (0.28)
G006.79-00.25	4.94	20.0	19.1, 21.0	7.89 (0.10)	3.47	9.35 (0.12)
	0.85	24.3	23.1, 25.4	1.80 (0.11)	3.47	2.13 (0.14)
G009.62+00.19	2.36	4.0	1.4, 6.3	11.92 (0.48)	5.15	31.13 (1.25)
G015.66-00.49	4.18	-7.2	-7.9, -6.6	4.45 (0.31)	4.55	9.04 (0.62)
	8.23	-5.3	-6.6, -4.1	12.04 (0.39)	4.55	24.44 (0.80)
G016.86-02.15	5.18	17.6	16.4, 18.9	17.92 (0.34)	2.35	9.70 (0.18)
G017.02-02.40	4.14	18.6	17.8, 19.5	7.49 (0.29)	1.88	2.61 (0.10)
	7.67	20.1	19.6, 21.1	8.17 (0.22)	1.88	2.85 (0.08)
	1.64	25.5	24.5, 26.3	1.75 (0.22)	1.88	0.61 (0.08)
	1.40	28.5	27.3, 29.9	2.24 (0.27)	1.88	0.78 (0.09)
G018.34+01.76	11.00	32.0	31.1, 33.1	12.85 (0.16)	2.00	5.05 (0.06)
	4.74	33.9	33.1, 34.4	4.45 (0.14)	2.00	1.75 (0.05)
G019.00-00.02	9.14	59.4	58.5, 60.9	17.76 (0.32)	4.05	28.60 (0.52)
G019.36-00.03	57.02	26.7	25.9, 27.9	121.90 (0.48)	2.84	96.68 (0.38)
G022.35+00.06	10.69	83.9	82.9, 84.3	8.46 (0.28)	4.33	15.58 (0.51)
G023.20-00.37	21.49	77.4	76.7, 77.9	24.94 (0.53)	4.18	42.90 (0.91)
G023.38+00.18	1.09	75.5	74.9, 76.4	1.27 (0.20)	4.81	2.89 (0.45)
	2.50	77.9	77.1, 78.9	2.39 (0.18)	4.81	5.43 (0.40)
G023.43-00.18	9.51	96.9	95.8, 97.9	13.08 (1.03)	5.30	36.11 (2.84)
	23.21	102.4	101.4, 103.5	44.26 (1.22)	5.30	122.17 (3.36)
G024.78+00.08	8.62	108.1	107.2, 109.0	11.01 (0.31)	6.67	48.06 (1.37)
	9.39	110.6	109.0, 111.7	18.50 (0.40)	6.67	80.78 (1.73)
	5.58	112.5	111.8, 112.9	6.54 (0.32)	6.67	28.54 (1.40)
	7.42	113.9	112.9, 115.1	15.41 (0.43)	6.67	67.30 (1.86)
G028.39+00.08	34.84	76.7	75.7, 78.0	44.82 (0.82)	4.33	82.54 (1.52)
	15.92	78.9	78.3, 80.2	41.31 (0.96)	4.33	76.08 (1.77)
G028.83-00.25	1.17	87.0	85.3, 89.2	4.43 (0.06)	5.00	10.88 (0.16)
G030.41-00.23	11.96	104.7	104.3, 105.3	16.55 (0.36)	3.95	25.41 (0.56)
G030.70-00.06	8.93	89.8	88.5, 90.7	14.27 (0.48)	6.54	59.88 (2.03)
	4.85	91.5	91.0, 92.2	6.72 (0.46)	6.54	28.19 (1.95)
	3.93	93.3	92.5, 94.4	8.77 (0.58)	6.54	36.83 (2.45)
G030.78+00.20	34.00	82.4	81.5, 83.2	30.11 (1.17)	7.14	150.94 (5.87)
G030.81-00.05	23.06	99.3	95.5, 101.64	147.11 (0.22)	3.12	140.3 (0.21)
G031.28+00.06	7.05	109.1	106.4, 112.0	31.45 (0.20)	4.76	70.03 (0.44)
G032.74-00.07	4.40	36.0	34.9, 36.8	6.09 (0.19)	7.94	37.69 (1.17)
	2.48	38.0	37.1, 38.8	4.74 (0.23)	7.94	29.37 (1.41)
	2.15	39.7	39.0, 40.7	3.21 (0.20)	7.94	19.85 (1.24)
G033.39+00.00	1.18	103.8	101.7, 105.9	4.57 (0.35)	8.85	35.17 (2.71)
G034.26+00.15	18.78	56.3	55.4, 57.3	25.99 (0.37)	3.41	29.69 (0.43)
G034.41+00.23	8.51	57.2	55.1, 60.4	30.48 (0.31)	2.94	25.91 (0.26)
G035.14-00.73	5.00	33.7	31.5, 36.4	18.84 (0.28)	2.19	8.88 (0.13)
G035.79-00.17	2.59	60.1	59.5, 60.6	4.52 (0.24)	8.85	34.81 (1.82)
	3.93	62.0	60.8, 63.1	7.11 (0.24)	8.85	54.72 (1.86)
	1.13	64.4	63.7, 65.4	2.41 (0.26)	8.85	18.52 (1.98)
G040.28-00.21	78.07	73.1	71.8, 74.2	99.72 (0.04)	3.37	111.10 (0.04)
	14.68	75.0	74.5, 75.9	20.32 (0.40)	3.37	22.64 (0.45)
G043.03-00.45	1.35	55.9	55.1, 56.7	1.73 (0.21)	7.69	10.03 (1.22)
	3.25	57.8	57.0, 59.1	6.24 (0.26)	7.69	36.26 (1.51)
G045.80-00.35	4.48	57.6	56.4, 58.5	7.15 (0.23)	7.30	37.46 (1.21)
	1.90	60.7	59.6, 61.5	2.63 (0.22)	7.30	13.78 (1.13)
	0.47	62.5	61.8, 63.6	0.50 (0.18)	7.30	2.63 (0.96)
G045.49+00.12	1.03	60.2	58.8, 60.8	1.76 (0.46)	6.94	8.36 (2.19)

**Table 6**  
(Continued)

Source Name	$S_p$ (Jy)	$V_p$ (km s <sup>-1</sup> )	$\Delta V$ (km s <sup>-1</sup> )	$S_{\text{int}}$ (Jy km s <sup>-1</sup> )	Distance (kpc)	$L$ (10 <sup>-6</sup> $L_{\odot}$ )
(1)	(2)	(3)	(4)	(5)	(6)	(7)
	0.73	62.1	61.5, 62.7	1.03 (0.44)	6.94	4.87 (2.06)
	1.33	63.8	63.0, 64.8	1.39 (0.32)	6.94	6.60 (1.50)
<b>G048.99-00.29</b>	34.98	66.1	66.0, 66.6	38.28 (1.11)	5.62	118.74 (3.43)
	46.51	67.3	66.9, 68.2	56.93 (1.18)	5.62	176.57 (3.65)
G049.04-01.07	1.63	39.1	37.6, 41.2	4.57 (0.42)	6.10	16.68 (1.54)
G049.26+00.31	0.74	0.7	-0.2, 1.3	0.94 (0.21)	8.85	7.24 (1.58)
	1.55	2.4	1.7, 3.4	1.65 (0.19)	8.85	12.69 (1.46)
	1.54	3.9	3.3, 5.5	3.09 (0.26)	8.85	23.76 (2.02)
G049.49-00.39	0.71	55.0	53.9, 55.9	1.13 (0.10)	5.13	2.93 (0.26)
	1.00	66.5	65.9, 67.2	1.27 (0.09)	5.13	3.29 (0.23)
G059.78+00.06	14.23	22.4	21.2, 23.6	12.82 (0.36)	2.16	5.88 (0.16)
G059.83+00.67	1.78	34.7	33.1, 36.1	3.90 (0.28)	4.13	6.54 (0.48)
G097.53+03.18	0.32	-71.9	-74.3, -70.9	1.02 (0.08)	7.52	5.69 (0.46)
	0.45	-68.8	-70.5, -67.4	1.04 (0.07)	7.52	5.79 (0.39)
G109.87+02.11	1.26	-10.6	-14.7, -7.5	5.09 (0.15)	0.81	0.33 (0.01)
	0.66	-5.7	-7.0, -4.1	2.37 (0.14)	0.81	0.15 (0.01)
G133.94+01.06	7.16	-46.7	-47.4, -44.3	27.37 (0.31)	1.96	10.33 (0.12)
G359.61-00.24	19.56	18.0	17.4, 18.7	22.90 (0.53)	2.67	16.00 (0.37)
	30.80	19.5	18.7, 20.0	32.78 (0.51)	2.67	22.91 (0.35)
	16.90	20.7	20.1, 21.6	18.34 (0.51)	2.67	12.82 (0.36)
W33	3.67	36.51	33.73, 39.04	24.99 (0.31)	3.67	27.39 (0.34)
WB89 171	1.77	-7.9	-9.0, -7.5	1.89 (0.09)	0.83	0.13 (0.01)
	2.01	-6.8	-7.5, -5.6	2.57 (0.10)	0.83	0.17 (0.01)

**Note.** The first 10 sources in bold style are newly detected CH<sub>3</sub>OH masers. Column (1): source name. Columns (2)–(4): the peak flux density, the line center velocity, and the velocity range. Column (5): the integrated flux density (in units of Jy km s<sup>-1</sup>). Column (6): the kinematic distance of our sources, measured by a maser parallax method (Reid et al. 2014, 2019). Column (7): the estimated maser luminosity, assuming its isotropic emission.

width of high- $J$  transitions ( $J = 8 \rightarrow 7$ ) is larger than that of low- $J$  transitions ( $J = 0 \rightarrow 1$ ). High- $J$  CH<sub>3</sub>OH transitions with larger line widths imply the inner regions (the locations of high- $J$  transitions) of molecular cloud cores suffer more violent turbulence or other motions than the outer regions (the locations of low- $J$  transitions), which is consistent with the results for HC<sub>3</sub>N (Feng et al. 2021).

### 3.3.2. Line Width–Bolometric Luminosity Relation

Previous research on NH<sub>3</sub> (Wouterloot et al. 1988; Myers et al. 1991; Ladd et al. 1994; Molinari et al. 1996; Jijina et al. 1999; Wu et al. 2006; Urquhart et al. 2011, 2015), C<sup>18</sup>O (Saito et al. 2001; Ridge et al. 2003; Maud et al. 2015), <sup>13</sup>CO (Wang et al. 2009; Lundquist et al. 2015), and H<sub>2</sub>CO (Tang et al. 2018) has reported that the molecular line width is correlated with the bolometric luminosity ( $L_{\text{bol}}$ ), which indicates a connection between the mass growth of the protostar and the internal velocity dispersion of the dense clump.

We investigated this relation for our sample between the line width of the CH<sub>3</sub>OH nonmasing emission line and  $L_{\text{bol}}$ , which were collected from Urquhart et al. (2018). Figure 4 presents our CH<sub>3</sub>OH line width as a function of  $L_{\text{bol}}$  and we can find apparent correlations for all transition lines, though there are large scatters. We performed a weighted least-squares linear fit to the log–log relationship between line width and  $L_{\text{bol}}$  and obtained a mean slope of  $\sim 0.11$  with correlation coefficients in the range of 0.67–0.98 (see Table 7). This is consistent with previous measurements on other molecules (Saito et al. 2001; Wang et al. 2009; Urquhart et al. 2015; Tang et al. 2018). This supports the previous proposition that there is a connection

**Table 7**  
Linear Fit Results for the Line Width of Detected CH<sub>3</sub>OH Lines and the Bolometric Luminosity

CH <sub>3</sub> OH Transitions (1)	Slope (2)	Intercept (3)	$R$ (4)	Sample Size (5)
8 <sub>0,8</sub> –7 <sub>1,7</sub> E	0.10 (0.03)	0.30 (0.13)	0.76	11
7 <sub>2,5</sub> –8 <sub>1,8</sub> A+	0.15 (0.04)	0.07 (0.21)	0.84	8
5 <sub>1,4</sub> –4 <sub>2,2</sub> E	0.12 (0.01)	0.17 (0.03)	0.98	12
4 <sub>2,2</sub> –3 <sub>1,2</sub> E	0.11 (0.02)	0.14 (0.12)	0.74	19
3 <sub>1,3</sub> –2 <sub>1,2</sub> A+	0.09 (0.01)	0.28 (0.07)	0.80	30
2 <sub>1,1</sub> –1 <sub>1,0</sub> A–	0.08 (0.02)	0.33 (0.10)	0.67	23
2 <sub>1,1</sub> –1 <sub>1,0</sub> E	0.09 (0.02)	0.28 (0.11)	0.67	21
2 <sub>1,2</sub> –1 <sub>1,1</sub> A+	0.07 (0.02)	0.38 (0.08)	0.67	22
0 <sub>0,0</sub> –1 <sub>-1,1</sub> E	0.16 (0.03)	-0.08 (0.15)	0.79	20

**Note.**  $R$  is the correlation coefficient.

between the protostar and the velocity dispersion of the dense clump gas, i.e., the mass growth of the protostar is determined by the internal velocity dispersion of the dense clump (Saito et al. 2001).

### 3.4. Column Density and Rotational Temperature

Due to the threefold symmetry of its hindering potential, CH<sub>3</sub>OH exists in  $A$ - and  $E$ -symmetry states. Since electric dipole transitions are forbidden between  $A$  and  $E$  levels and  $A$ -type and  $E$ -type CH<sub>3</sub>OH have independent rotation spectra (Ball et al. 1970; Menten et al. 1988; Leurini 2005; Wirström et al. 2011), we performed rotational diagram analysis for these two species separately, i.e., separately for  $A$ -type and  $E$ -type

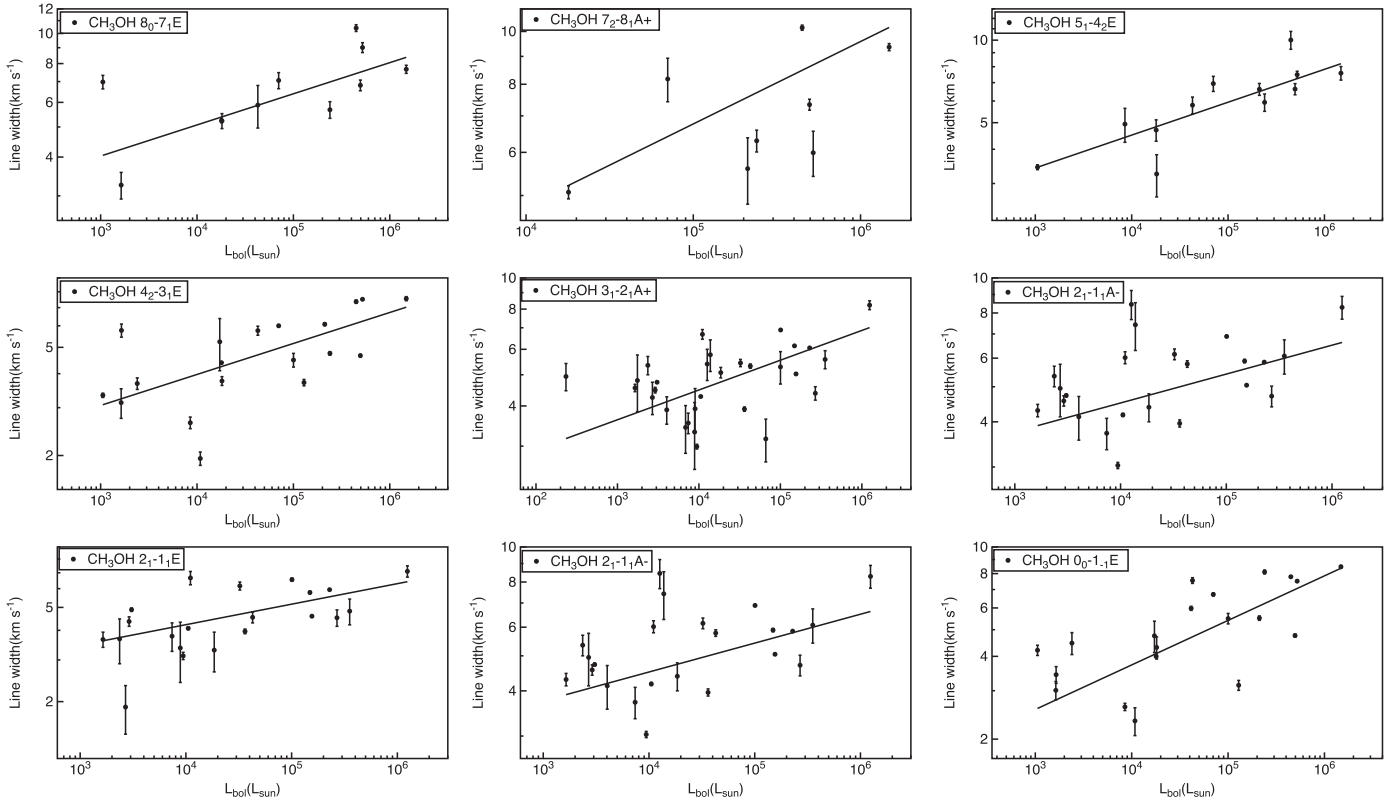


**Figure 4.** The line width of the CH<sub>3</sub>OH transition lines vs. the bolometric luminosity, with solid lines for the linear fit.

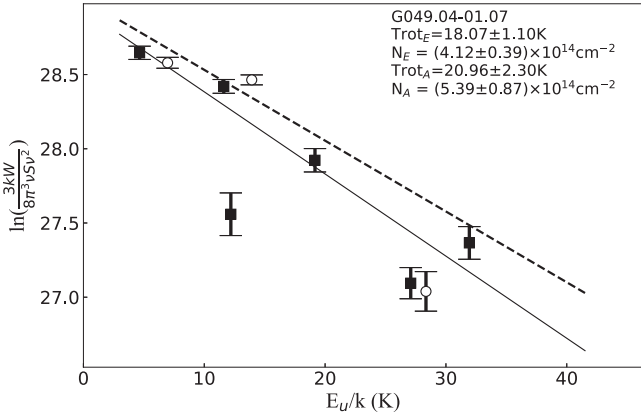


**Figure 5.** The CH<sub>3</sub>OH rotational diagram of our 111 sources. The solid line is the fit to the *E*-type CH<sub>3</sub>OH (solid squares) and the dashed line to the *A*-type CH<sub>3</sub>OH (empty circles). The fit results are shown in the upper right corner. (The complete figure set (111 images) is available.)

CH<sub>3</sub>OH lines, in order to estimate their rotation temperatures and column densities.

Under the conditions of optical thin lines and local thermodynamic equilibrium, the following equation is used for the analysis of the rotational diagram (Goldsmith & Langer 1999):

$$\ln\left(\frac{3kW}{8\pi^3\nu S\mu^2}\right) = \ln\left[\frac{N(T_{\text{rot}} - T_{\text{bg}})}{QT_{\text{rot}}}\right] - \frac{E_u}{kT_{\text{rot}}}, \quad (2)$$

where  $k$  is the Boltzmann constant,  $W$  is the integrated line intensity, and  $\nu$  is the rest frequency of the transition.  $T_{\text{rot}}$  is the rotational temperature and  $T_{\text{bg}} \approx 2.73$  K is the background

temperature.  $E_u/k$  and  $S\mu^2$  are the upper-level energy and the square of the electric dipole moment, respectively. The values of  $E_u/k$  and  $S\mu^2$  are listed in Table 2. We used the partition function ( $Q$ ) for CH<sub>3</sub>OH in our analyses (Townes & Schawlow 1955; Purcell et al. 2009):

$$Q(T) = \sum_{J=0}^{\infty} (2J+1)e^{-E_J/kT} \approx 1.2327T_{\text{rot}}^{1.5}. \quad (3)$$

For the 111 sources with the number of detected CH<sub>3</sub>OH nonmasing emission lines  $\geq 2$  and the separation of adjacent  $E_u/k > 10$  K for each type, we performed rotational diagram fitting. The obtained rotation temperature and column density are summarized in Table 8 and the rotational diagrams with the fit lines and corresponding results are presented in Figure 5. Figure 6 (left panel) presents the column density distribution of *A*-type and *E*-type CH<sub>3</sub>OH. It shows clearly that the column density of *E*-type CH<sub>3</sub>OH is lower than that of *A*-type CH<sub>3</sub>OH. We further calculated the column density ratio of CH<sub>3</sub>OH ( $N(\text{CH}_3\text{OH})$ ) and H<sub>2</sub> ( $N(\text{H}_2)$ ), i.e., the relative abundance of CH<sub>3</sub>OH ( $X(\text{CH}_3\text{OH})$ ) for those two types (Table 8). A similar trend can be found (right panel of Figure 6), i.e., *A*-type CH<sub>3</sub>OH tends to have larger abundance.

Meanwhile, some uncertainties have to be mentioned for our rotation analysis results. First, the frequency of our targeted CH<sub>3</sub>OH lines ranges from 90 to 224 GHz, which may bring the beam dilution effect on the rotation diagram analysis. We investigated CH<sub>3</sub>OH mapping observations (e.g., Jones et al. 2008; Gómez et al. 2011; Watanabe et al. 2017; Liu et al. 2020) for our sources. We got the size for dozens of sources and found that all of them are larger than 25'' at the 3 mm band (e.g., G133.94 +01.06, G000.67–00.03, G009.62+00.19, G011.10–00.11, and

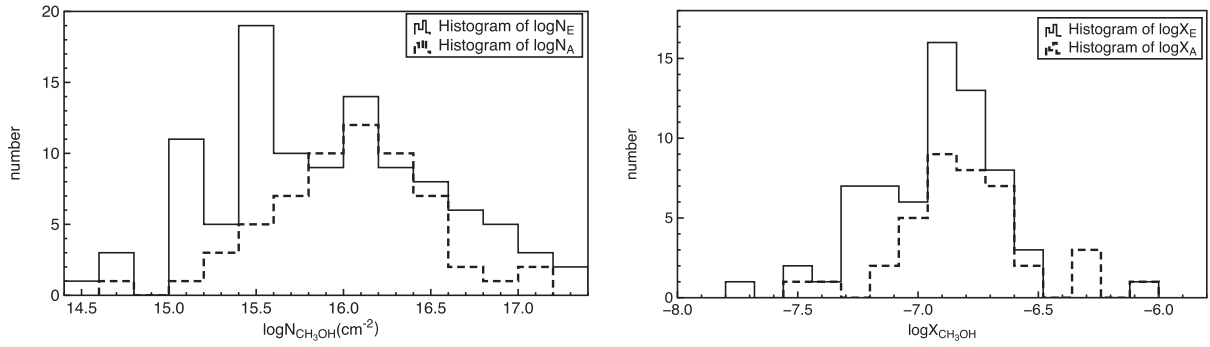


**Figure 6.** Distributions of the column density (left panel) and the relative abundance (right panel) for *A*-type (dashed lines) and *E*-type  $\text{CH}_3\text{OH}$  (solid lines) in our sample.

**Table 8**  
Measured Parameters of *A*-type and *E*-type  $\text{CH}_3\text{OH}$

Source Name	$\text{CH}_3\text{OH}$ <i>E</i> -type			$\text{CH}_3\text{OH}$ <i>A</i> -type			<i>E/A</i>
	$T_{\text{rot}}$ (K)	$N$ ( $10^{14} \text{ cm}^{-2}$ )	$X$ ( $10^{-9}$ )	$T_{\text{rot}}$ (K)	$N$ ( $10^{14} \text{ cm}^{-2}$ )	$X$ ( $10^{-9}$ )	
(1)	(2)	(3)	(4)	(5)	(6)	(7)	(8)
G000.31–00.20	21.09 (1.98)	3.79 (0.53)	...	31.43 (1.49)	9.32 (0.68)	...	0.41
G000.37+00.03	18.41 (0.19)	12.99 (0.30)	...	24.76 (0.46)	26.47 (0.86)	...	0.49
G000.67–00.03	36.02 (0.41)	154.17 (3.46)	...	...	...	...	...
G001.00–00.23	9.54 (0.67)	5.80 (0.61)	...	...	...	...	...
G001.14–00.12	27.02 (1.59)	13.24 (1.24)	...	...	...	...	...
G002.70+00.04	12.22 (0.40)	5.21 (0.30)	...	...	...	...	...
G005.88–00.39	56.53 (1.61)	41.46 (1.85)	13.45 (0.60)	...	...	...	...
G006.79–00.25	14.61 (0.17)	12.43 (0.28)	11.47 (0.26)	9.64 (0.08)	12.88 (0.26)	11.88 (0.24)	0.96

**Note.** Column (1): source name. Columns (2)–(4): parameters of *E*-type  $\text{CH}_3\text{OH}$ : rotation temperature, column density, and  $X(\text{CH}_3\text{OH})$ . Columns (5)–(7): the same parameters of *A*-type  $\text{CH}_3\text{OH}$ . Column (8): the column density ratio of *E/A*.

(This table is available in its entirety in machine-readable form.)

G049.49–00.39), which is the biggest beam size (see details in Table 1). Thus the beam dilution effect should not be significant on our measurements. Another important factor is the assumption of optical thinness for the  $\text{CH}_3\text{OH}$  lines, since such lines are sometimes optically thick (e.g., Bisschop et al. 2007; Rivilla et al. 2017; van Gelder et al. 2022). Thanks to the broad bandwidth of IRAM 30 m,  $^{13}\text{CH}_3\text{OH}$  lines are also covered in our observations. For 17 sources matching the criteria (the same as those for  $\text{CH}_3\text{OH}$ , i.e., more than two lines and a separation of adjacent  $E_u/k$  that is larger than 10 K), we performed rotation diagram analysis (Figure 7) and obtained their  $^{13}\text{CH}_3\text{OH}$  column densities. Further we estimated their  $^{12}\text{CH}_3\text{OH}$  column densities, according to the  $^{12}\text{C}/^{13}\text{C}$  gradient reported recently (Yan et al. 2019). Comparisons show that the values of  $\text{CH}_3\text{OH}$  column density from  $^{13}\text{CH}_3\text{OH}$  data are mostly larger than those derived directly from  $\text{CH}_3\text{OH}$  spectral data by the rotational diagram method (Table 9). It means that  $\text{CH}_3\text{OH}$  lines in our sources are likely to be optically thick and the results for  $\text{CH}_3\text{OH}$  column density directly from  $\text{CH}_3\text{OH}$  spectral data are likely to be the lower limit of the real column density of  $\text{CH}_3\text{OH}$ .

## 4. Discussion

### 4.1. Comparisons of Sources with and without Detected $\text{CH}_3\text{OH}$ Lines

It is interesting to investigate possible physical differences between sources with and without detections of  $\text{CH}_3\text{OH}$

lines, which may provide clues on the absence or rarity of  $\text{CH}_3\text{OH}$  line detections in some specific environments. We checked those physical parameters ( $L_{\text{bol}}$ , dust temperature ( $T_{\text{dust}}$ ), and  $N(\text{H}_2)$ ), from the APEX Telescope Large Area Survey of the Galaxy (ATLASGAL) catalog; see details in Section 4.2) for sources with and without detections of  $\text{CH}_3\text{OH}$  lines. However, only one source (G048.60+00.02) among the 27 sources without detected  $\text{CH}_3\text{OH}$  lines was found in ATLASGAL, which could not provide a basis for reliable statistical analysis. Thus we turned to investigate the relation between the number of detected  $\text{CH}_3\text{OH}$  lines and physical parameters.

Among the 148 sources with detections of  $\text{CH}_3\text{OH}$  lines, 90 were found in ATLASGAL. For comparison, we classified them into two groups, i.e., sources with detected  $\text{CH}_3\text{OH}$  lines less than 10 and sources with more than 10  $\text{CH}_3\text{OH}$  lines. We plot the distributions of  $L_{\text{bol}}$ ,  $T_{\text{dust}}$ ,  $N(\text{H}_2)$ , and  $N(\text{CH}_3\text{OH})$  for these two types of sources in Figure 8. No obvious differences in the distributions of  $L_{\text{bol}}$  and  $T_{\text{dust}}$  (upper panels) exist between them; however, significant differences can be found in the distributions of both  $N(\text{H}_2)$  and  $N(\text{CH}_3\text{OH})$  between the two samples (lower panels). Sources with more than 10  $\text{CH}_3\text{OH}$  lines tend to have higher gas column density than sources with less than 10 lines. Similar results can be found between sources with and without detections of  $\text{CH}_3\text{OH}$  masers (Figure 9), i.e., sources without obvious differences in  $L_{\text{bol}}$  and  $T_{\text{dust}}$  (upper panels), while sources with  $\text{CH}_3\text{OH}$  masers tend to

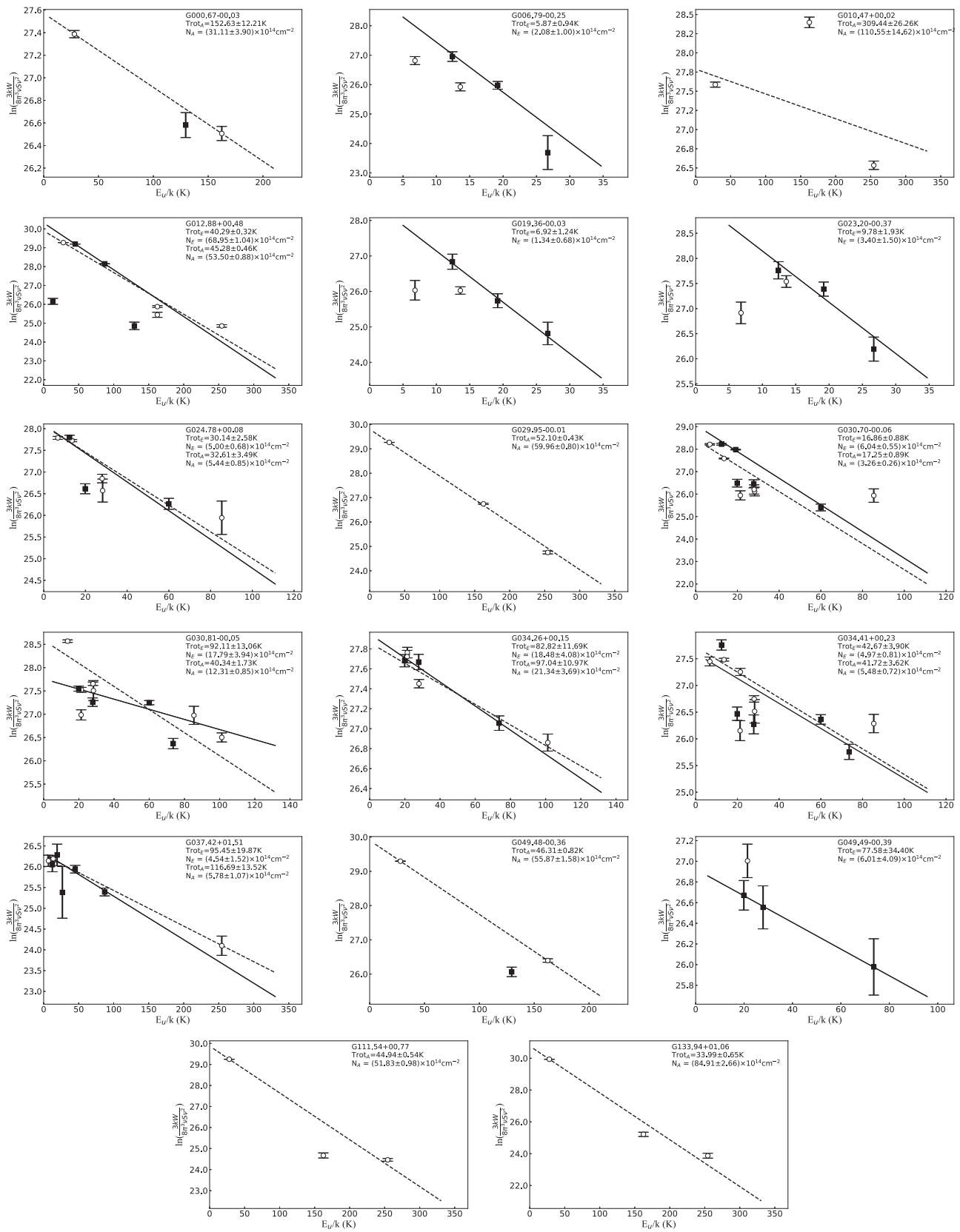
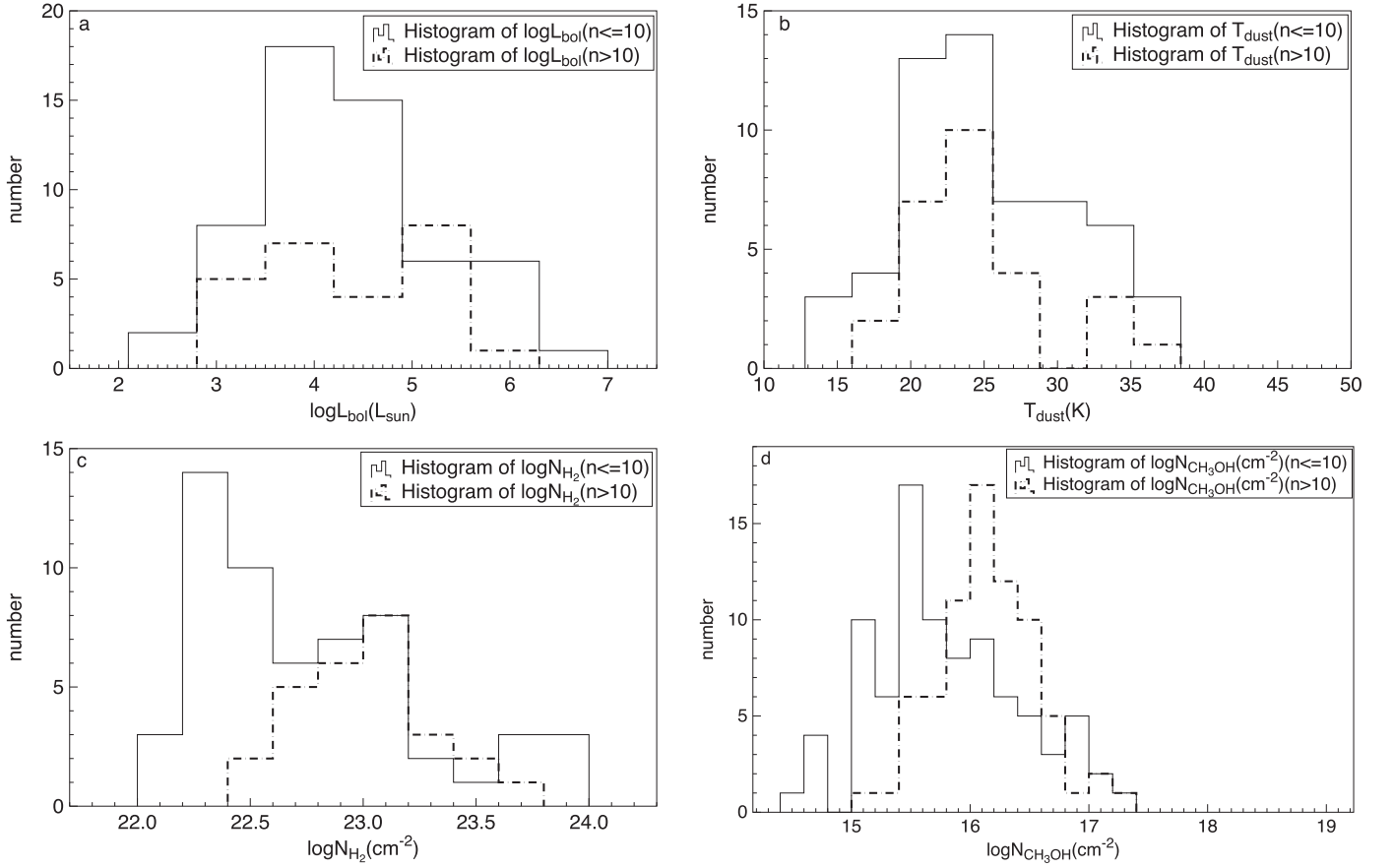


Figure 7. The  $^{13}\text{CH}_3\text{OH}$  rotational diagram of our sample. The solid line is the fit to the E-type  $^{13}\text{CH}_3\text{OH}$  (solid squares) and the dashed line to the A-type  $^{13}\text{CH}_3\text{OH}$  (empty circles). The fit results are shown in the upper right corner.



**Figure 8.** The histograms show the distribution of  $\log L_{\text{bol}}$ ,  $T_{\text{dust}}$ ,  $\log N_{\text{H}_2}$ , and  $\log N_{\text{CH}_3\text{OH}}$  for sources with detections of less than 10 (solid lines) and more than 10  $\text{CH}_3\text{OH}$  lines (dashed lines).

**Table 9**  
Measured Column Densities of  $^{13}\text{CH}_3\text{OH}$  and  $\text{CH}_3\text{OH}$  toward Our Sample

Source Name	$^{12}\text{C}/^{13}\text{C}$	The Column Density of E-type			The Column Density of A-type		
		$^{13}\text{CH}_3\text{OH}$ ( $10^{14} \text{ cm}^{-2}$ )	$\text{CH}_3\text{OH}$ (13) ( $10^{14} \text{ cm}^{-2}$ )	$\text{CH}_3\text{OH}$ (12) ( $10^{14} \text{ cm}^{-2}$ )	$^{13}\text{CH}_3\text{OH}$ ( $10^{14} \text{ cm}^{-2}$ )	$\text{CH}_3\text{OH}$ (13) ( $10^{14} \text{ cm}^{-2}$ )	$\text{CH}_3\text{OH}$ (12) ( $10^{14} \text{ cm}^{-2}$ )
(1)	(2)	(3)	(4)	(5)	(6)	(7)	(8)
G034.41+00.23	42.04	4.97 (0.81)	209.00 (65.30)	52.92 (0.91)	5.48 (0.72)	230.21 (71.93)	32.84 (0.57)
G030.70-00.06	33.04	6.04 (0.55)	199.51 (67.54)	41.93 (1.01)	3.26 (0.26)	107.85 (36.51)	31.78 (0.82)
G030.81-00.05	40.71	17.79 (3.94)	724.41 (228.60)	112.24 (1.74)	12.31 (0.85)	501.31 (158.19)	102.71 (1.01)
G024.78+00.08	29.54	5.00 (0.68)	147.59 (52.10)	238.24 (11.71)	5.44 (0.85)	160.62 (56.71)	39.62 (0.98)
G012.88+00.48	41.02	68.95 (1.04)	2828.39 (890.46)	22.59 (0.35)	53.50 (0.88)	2194.66 (690.94)	...
G037.42+01.51	46.05	4.54 (1.52)	208.96 (63.54)	24.48 (0.83)	5.78 (1.07)	266.37 (81.00)	9.60 (0.22)
G034.26+00.15	35.84	18.48 (4.08)	662.43 (217.97)	169.37 (1.59)	21.34 (3.69)	764.64 (251.60)	78.82 (4.43)
G006.79-00.25	35.74	2.08 (1.00)	74.35 (24.49)	12.43 (0.28)	...	12.88 (0.26)	...
G019.36-00.03	39.95	1.34 (0.68)	53.69 (17.04)	11.71 (0.32)	...	...	13.71 (0.36)
G023.20-00.37	35.18	3.40 (1.50)	119.73 (39.65)	50.39 (3.51)	...	...	25.27 (1.65)
G049.49-00.39	25.63	6.01 (4.09)	153.99 (57.57)	90.07 (19.80)	...	...	...
G029.95-00.01	35.33	...	...	34.13 (0.98)	59.96 (0.80)	2118.24 (700.41)	...
G049.48-00.36	43.25	...	...	64.04 (1.73)	55.87 (1.58)	2416.78 (748.60)	...
G111.54+00.77	59.71	...	...	15.94 (0.23)	51.83 (0.98)	3095.25 (879.22)	...
G133.94+01.06	60.53	...	...	74.32 (1.58)	84.91 (2.66)	5139.28 (1455.18)	...
G000.67-00.03	13.79	...	...	154.17 (3.46)	31.11 (3.90)	429.04 (218.34)	...
G010.47+00.02	19.89	...	...	132.27 (1.91)	110.55 (14.62)	2198.40 (921.75)	...

**Note.** Column (1): source name. Column (2): these values were calculated by the formula  $^{12}\text{C}/^{13}\text{C} = (5.08 \pm 1.10) \times D_{\text{GC}} + (11.86 \pm 6.60)$  (Yan et al. 2019). Columns (3)–(5): for E-type  $\text{CH}_3\text{OH}$ , the column density of  $^{13}\text{CH}_3\text{OH}$ , the column density of  $\text{CH}_3\text{OH}$  from the  $^{13}\text{CH}_3\text{OH}$  column density (times  $^{12}\text{C}/^{13}\text{C}$  in column (2)), and the column density of  $\text{CH}_3\text{OH}$  directly from  $^{12}\text{CH}_3\text{OH}$  spectral data by the rotation diagram method (Section 3.4). Columns (6)–(8): the same as columns (3)–(5) but for A-type  $\text{CH}_3\text{OH}$ .

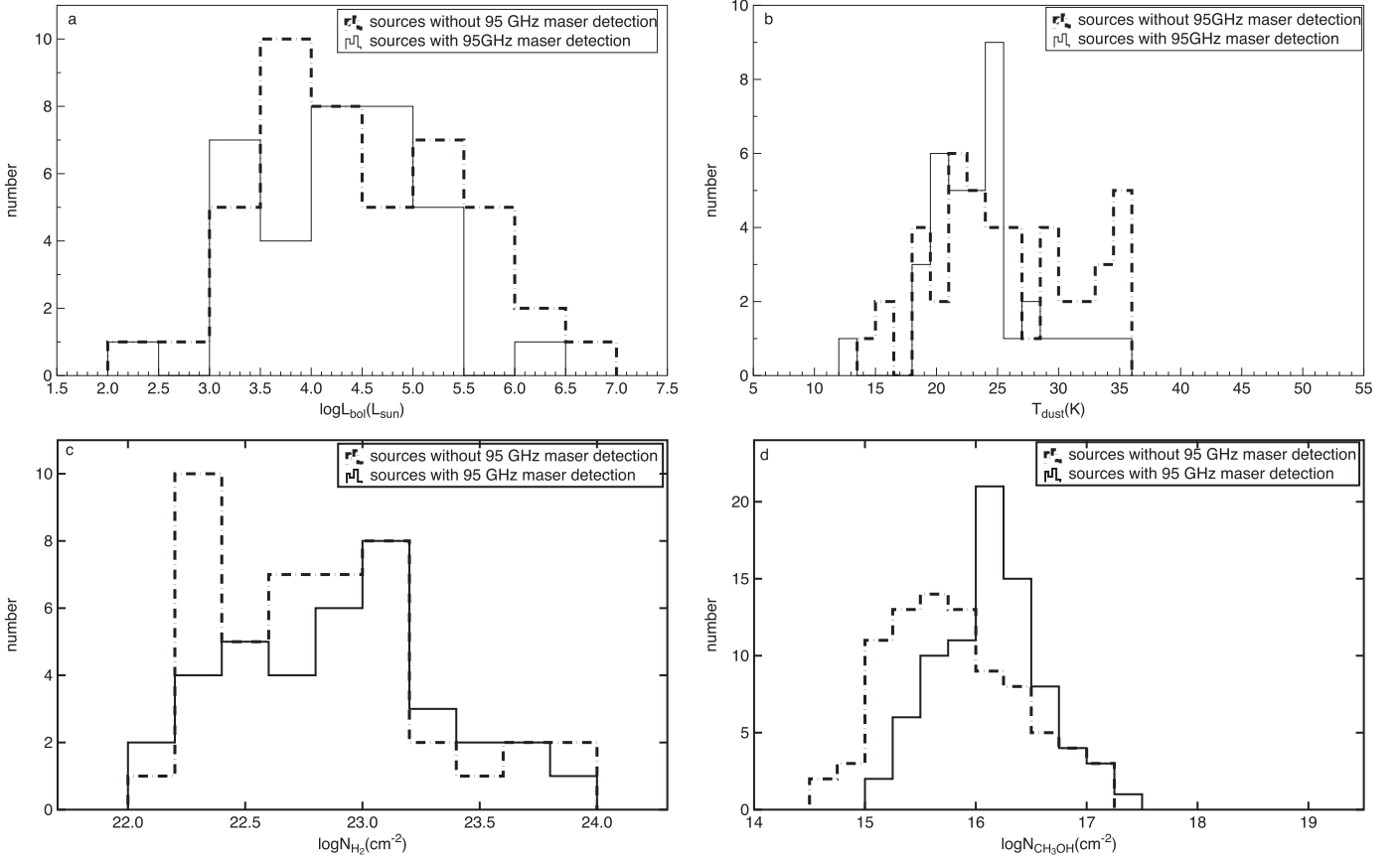


**Figure 9.** The histograms show the distribution of  $\log L_{\text{bol}}$ ,  $T_{\text{dust}}$ ,  $\log N_{\text{H}_2}$ , and  $\log N_{\text{CH}_3\text{OH}}$  for sources without (dashed lines) and with detections of 95 GHz CH<sub>3</sub>OH masers (solid lines).

have higher gas column density (lower panels). It is reasonable that both thermal and maser lines of CH<sub>3</sub>OH need a gas environment with high column density. And  $T_{\text{dust}}$  seems to be a nonsignificant factor for the production of either line.

#### 4.2. Ratio of E/A of Column Density of CH<sub>3</sub>OH

Previous studies have suggested that the successive hydrogenation of CO on interstellar dust is a key process in the production of CH<sub>3</sub>OH (Charnley et al. 1997; Woon 2002). Recently, more experiments have shown that hydrogenation on CO–H<sub>2</sub>O mixed ice is also very efficient for the production of CH<sub>3</sub>OH. And the most effective temperatures are about 10–15 K on CO:H<sub>2</sub>O ice mixtures or pure solid CO (Watanabe & Kouchi 2002; Watanabe et al. 2003, 2004). For CH<sub>3</sub>OH, its ground state of *E* type ( $J, K = 1, -1$ ) is about 7.9 K above the *A*-type ground state ( $J, K = 0, 0$ ), causing an overabundance of *A*-CH<sub>3</sub>OH created in a thermalized population distribution at a low temperature. Under this assumption, the abundance ratio  $E/A$  should change with the temperature and a low ratio value appears at low temperatures due to the overabundance of *A*-type CH<sub>3</sub>OH by then. Theoretical works have found that the  $E/A$  ratio of CH<sub>3</sub>OH really increases with increasing spin temperature ( $T_{\text{spin}}$ ) and tends to be stable with a value of  $\sim 1.0$  at  $T_{\text{spin}} \geq 37$  K (Wirström et al. 2011).  $T_{\text{spin}}$  describes the relative population temperature of a molecule with a noninteracting spin type and if it reflects the formation temperature of CH<sub>3</sub>OH, then measurement of the  $E/A$  ratio provides another observational test of the hypothesis that interstellar CH<sub>3</sub>OH forms from CO on cold grain surfaces (Wirström et al. 2011).

We calculated the  $E/A$  ratio for our sample, based on our results of the column density of *A*-type and *E*-type CH<sub>3</sub>OH (see details in Table 8). The majority of them (about 70%) have a ratio value less than 1.0, with a peak value of  $\sim 0.6$  (see Figure 10(a)). The relatively small values of the  $E/A$  ratio are consistent with theoretical predictions. In addition, the  $E/A$  ratio was plotted against  $N(\text{H}_2)$  (Urquhart et al. 2018) for our sample (Figure 10(b)). One remarkably positive correlation can be found between them and the least-squares linear fit gives  $E/A = (0.84 \pm 0.16) \times \log N_{\text{H}_2} + (-18.43 \pm 3.86)$ , with a correlation coefficient of 0.68. This is consistent with the previous prediction that a low  $E/A$  ratio appears at low temperature, assuming a positive correlation of the excitation temperature ( $T_{\text{ex}}$ ) to  $N(\text{H}_2)$ . All these support the hypothesis that interstellar CH<sub>3</sub>OH forms from CO on cold grain surfaces. Moreover, such consistency between our  $E/A$  ratio results and theoretical predictions suggests that the assumption of optical thinness has no significant effect on our measured  $E/A$  ratio.

#### 4.3. CH<sub>3</sub>OH Abundance versus Evolutionary Indicators

Recent studies have suggested that the excitation and abundance of CH<sub>3</sub>OH may be good evolutionary indicators during the embedded stage of star formation (van der Tak et al. 2000; Leurini 2005; Gerner et al. 2014). Considering  $T_{\text{dust}}$ ,  $L_{\text{bol}}$ , the mass of the dense clump ( $M_{\text{clump}}$ ), and  $N(\text{H}_2)$  are also used as evolutionary indicators for HMSFRs (Elia et al. 2017; König et al. 2017; Urquhart et al. 2018, 2022), we investigated the relations between these evolutionary indicators and CH<sub>3</sub>OH abundance toward our sample.

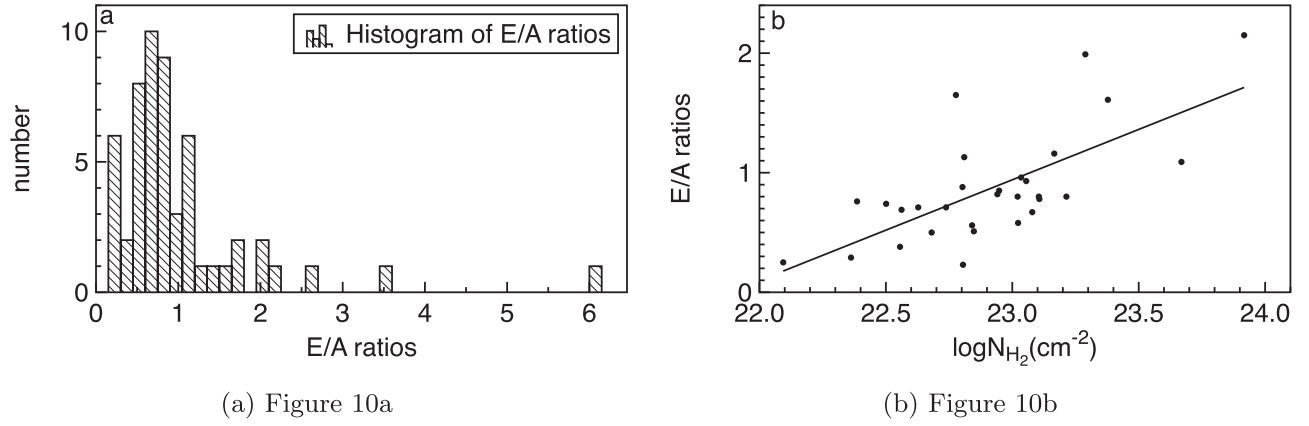


**Figure 10.** (a) Histogram of the column density ratios of *E*-type and *A*-type  $\text{CH}_3\text{OH}$  and (b) the *E/A* ratio against the column density of  $\text{H}_2$  for our sample.

**Table 10**  
Evolutionary Indicators and  $\text{CH}_3\text{OH}$  Abundance of Our Sample

Source Name	$T_{\text{dust}}$ (K)	$\log M_{\text{clump}}$ ( $M_{\text{Sun}}$ )	$\log L_{\text{bol}}$ ( $L_{\text{Sun}}$ )	$\log N_{\text{H}_2}$ ( $\text{cm}^{-2}$ )	$N_{E\text{-type}}$ ( $10^{14} \text{cm}^{-2}$ )	$X_{E\text{-type}}$ ( $10^{-9}$ )	$N_{A\text{-type}}$ ( $10^{14} \text{cm}^{-2}$ )	$X_{A\text{-type}}$ ( $10^{-9}$ )
(1)	(2)	(3)	(4)	(5)	(6)	(7)	(8)	(9)
G006.79–00.25	22.4	2.985	3.974	23.035	12.43 (0.28)	11.47 (0.26)	12.88 (0.26)	11.88 (0.24)
G009.62+00.19	32.1	3.523	5.379	23.214	21.18 (0.43)	12.94 (0.26)	26.64 (2.06)	16.28 (1.26)
G010.32–00.15	32.1	3.321	5.429	22.777	9.62 (1.09)	16.08 (1.82)	5.84 (0.22)	9.76 (0.37)
G015.66–00.49	19.4	...	...	...	10.79 (0.71)	15.31 (1.01)	21.34 (1.61)	30.28 (2.28)
G017.63+00.15	34.6	2.395	4.515	22.805	1.28 (0.23)	2.01 (0.36)	5.66 (0.82)	8.87 (1.28)
G019.00–00.02	23.9	3.202	4.102	22.681	10.83 (0.64)	22.58 (1.33)	21.78 (1.69)	45.40 (3.52)
G019.36–00.03	19.5	2.851	3.463	22.948	11.71 (0.32)	13.20 (0.36)	13.71 (0.36)	15.45 (0.41)
G023.20–00.37	20.1	3.442	4.043	23.289	50.39 (3.51)	25.90 (1.80)	25.27 (1.65)	12.99 (0.85)
G023.43–00.18	24.6	3.756	4.631	23.107	20.42 (0.36)	15.96 (0.28)	26.15 (0.57)	20.44 (0.45)
G024.78+00.08	26.5	3.883	5.173	23.418	238.24 (11.71)	90.99 (4.47)	39.62 (0.98)	15.13 (0.37)
G028.14–00.00	22.2	3.203	3.947	22.628	7.04 (0.33)	16.58 (0.78)	9.98 (1.37)	23.50 (3.23)
G028.39+00.08	18.5	3.517	4.022	23.166	26.13 (0.15)	17.83 (0.10)	22.54 (0.32)	15.38 (0.22)
G028.83–00.25	24.6	3.338	4.559	22.941	8.22 (0.09)	9.42 (0.10)	9.99 (0.08)	11.44 (0.09)
G030.41–00.23	20.3	3.529	4.268	23.055	16.45 (0.92)	14.49 (0.81)	17.67 (0.88)	15.57 (0.78)
G030.70–00.06	24.2	4.047	5.192	23.424	41.93 (1.01)	15.80 (0.38)	31.78 (0.82)	11.97 (0.31)
G030.74–00.04	35.4	3.357	5.549	22.760	3.88 (0.61)	6.74 (1.06)	1.94 (0.18)	3.37 (0.31)
G030.78+00.20	20.9	3.139	3.869	22.921	9.98 (0.34)	11.97 (0.41)	10.91 (0.39)	13.09 (0.47)
G030.81–00.05	25.1	4.084	5.359	23.669	112.24 (1.74)	24.05 (0.37)	102.71 (1.01)	22.01 (0.22)
G030.97–00.14	14.8	3.613	3.836	22.841	4.01 (0.39)	5.78 (0.56)	7.18 (0.69)	10.35 (1.00)
G031.28+00.06	24.7	3.649	4.841	23.105	15.67 (0.39)	12.30 (0.31)	19.56 (0.92)	15.36 (0.72)
G033.64–00.22	27.9	2.748	4.069	22.362	1.58 (0.24)	6.87 (1.04)	5.43 (0.62)	23.59 (2.69)
G034.26+00.15	29.2	3.234	4.788	23.917	169.37 (1.59)	20.50 (0.19)	78.82 (4.43)	9.54 (0.54)
G034.41+00.23	22.7	2.587	3.486	23.378	52.92 (0.91)	22.16 (0.38)	32.84 (0.57)	13.75 (0.24)
G034.79–01.38	18.9	2.825	3.216	23.023	11.70 (0.53)	11.10 (0.50)	20.01 (0.84)	10.91 (0.43)
G035.79–00.17	19.6	2.789	3.373	22.810	10.03 (0.41)	15.53 (0.64)	8.91 (0.41)	13.80 (0.64)
G038.03–00.30	22.3	2.978	3.801	22.094	2.98 (0.21)	24.00 (1.69)	11.78 (1.49)	94.87 (12.00)
G040.28–00.21	24.6	3.343	4.510	23.079	38.42 (1.02)	32.03 (0.85)	57.68 (1.94)	48.09 (1.62)
G040.42+00.70	26.7	3.608	4.821	22.402	3.11 (0.55)	12.32 (2.18)	3.67 (0.81)	14.54 (3.21)
G040.62–00.13	26.0	3.682	5.001	22.738	4.57 (0.21)	8.35 (0.38)	6.41 (0.54)	11.72 (0.99)
G043.03–00.45	23.7	...	...	...	8.17 (0.44)	12.86 (0.69)	9.31 (0.48)	14.65 (0.76)
G045.80–00.35	26.5	2.662	3.953	22.458	3.70 (0.50)	12.89 (1.74)	5.72 (0.96)	19.92 (3.34)
G049.04–01.07	24.0	2.229	3.245	22.386	4.12 (0.39)	16.94 (1.60)	5.39 (0.87)	22.16 (3.58)
G049.26+00.31	12.9	3.064	2.368	22.562	6.86 (0.36)	18.81 (0.99)	9.95 (0.96)	27.28 (2.63)
G054.10–00.08	26.5	2.987	3.605	22.556	6.16 (0.58)	17.12 (1.61)	16.08 (0.95)	44.70 (2.64)
G058.77+00.64	28.1	1.993	3.429	22.501	4.89 (0.29)	15.43 (0.91)	6.64 (0.61)	20.95 (1.92)
G059.78+00.06	23.6	2.866	3.930	23.021	6.35 (0.19)	6.05 (0.18)	7.92 (0.23)	7.55 (0.22)

**Note.** Taken from the ATLASGAL catalog (Urquhart et al. 2018). Column (1): source name. Column (2): dust temperature. Column (3): log of the clump mass. Column (4): log of the bolometric luminosity. Column (5): log of the  $\text{H}_2$  column density. Columns (6)–(9): the column density and relative abundance for *E*-type and *A*-type  $\text{CH}_3\text{OH}$ , taken from Table 8.

Using a search radius of  $25''$ , we crossmatched our sample with the ATLASGAL catalog of  $870 \mu\text{m}$  continuum clumps (Urquhart et al. 2018) and got data on those indicators, i.e.,

$T_{\text{dust}}$ ,  $L_{\text{bol}}$ ,  $N(\text{H}_2)$ , and  $M_{\text{clump}}$  (see details in Table 10). No significant correlations could be found between  $L_{\text{bol}}$ ,  $M_{\text{clump}}$ , and  $\text{CH}_3\text{OH}$  abundance for our sample. Figure 11 (upper

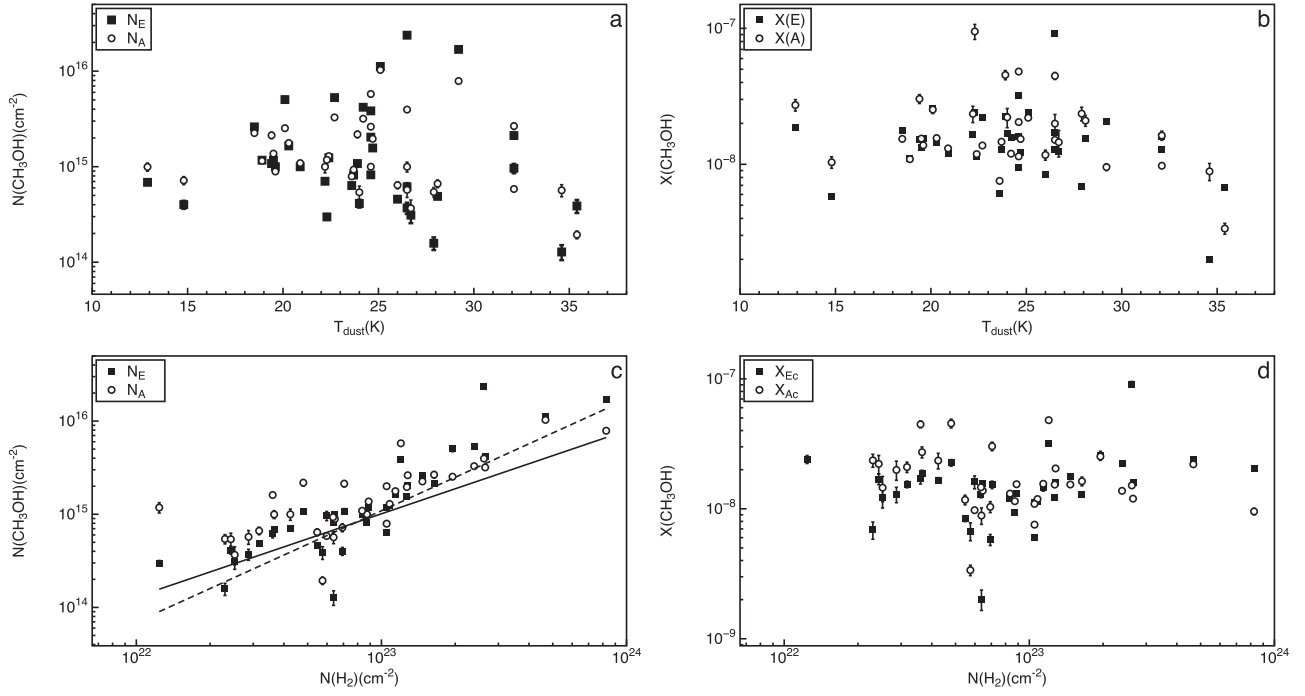


**Figure 11.**  $N(\text{CH}_3\text{OH})$  and  $X(\text{CH}_3\text{OH})$  against  $T_{\text{dust}}$  (upper panels) and against  $N(\text{H}_2)$  (lower panels) for our  $E$ -type (squares) and  $A$ -type  $\text{CH}_3\text{OH}$  sources (empty circles). The solid line is the fit to the  $E$ -type  $\text{CH}_3\text{OH}$  and the dashed line to the  $A$ -type  $\text{CH}_3\text{OH}$ .

panels) presents the relations of  $N(\text{CH}_3\text{OH})$  and  $X(\text{CH}_3\text{OH})$  to  $T_{\text{dust}}$ . It shows clearly a decreasing trend of  $\text{CH}_3\text{OH}$  abundance beyond  $\sim 30$  K in both panels. This is basically consistent with theoretical results. Around 20–30 K,  $\text{CH}_3\text{OH}$  ice photolysis could happen and lead to an enhancement of gas-phase  $\text{CH}_3\text{OH}$  abundance by up to 1 order of magnitude via chemical desorption. This effect would be weak beyond 30 K, because at low temperatures, recombination of dissociated  $\text{CH}_3\text{OH}$  is more efficient than that at higher temperatures (Rocha et al. 2023). This also supports the fact that  $\text{CH}_3\text{OH}$  is easily formed in low-temperature environments.

In addition,  $N(\text{H}_2)$  is plotted against the  $\text{CH}_3\text{OH}$  abundance ( $N(\text{CH}_3\text{OH})$ ,  $X(\text{CH}_3\text{OH})$ ) for our sample in Figure 11 (lower panels). A strong correlation can be found between  $N(\text{CH}_3\text{OH})$  and  $N(\text{H}_2)$ . The weighted least-squares linear fit gives

$$\log N_E = (0.89 \pm 0.14) \times \log N_{\text{H}_2} + (-5.53 \pm 3.13) \quad (4)$$

$$\log N_A = (1.19 \pm 0.21) \times \log N_{\text{H}_2} + (-12.44 \pm 4.87) \quad (5)$$

with correlation coefficients of 0.74 and 0.69 for  $E$ -type and  $A$ -type  $\text{CH}_3\text{OH}$ , respectively. No significant correlation could be found between  $X(\text{CH}_3\text{OH})$  and  $N(\text{H}_2)$ .  $X(\text{CH}_3\text{OH})$  is kept constant with the change of  $N(\text{H}_2)$ , indicating that  $\text{CH}_3\text{OH}$  is a reliable tracer of  $N(\text{H}_2)$ . A similar distribution was found for the column density ratio of  $\text{H}_2\text{CO}$  with  $\text{H}_2$  toward a sample of HMSFRs (Tang et al. 2018), which is consistent with the fact that both  $\text{CH}_3\text{OH}$  and  $\text{H}_2\text{CO}$  have similar formation processes, i.e., formation from conventional hydrogenation on grain surfaces.

## 5. Summary

In this work, we have presented a line survey of multi-transition  $\text{CH}_3\text{OH}$  toward a large sample of 175 HMSFRs with the IRAM 30 m telescope in the 3 mm, 2 mm, and 1.3 mm bands. Our main results are summarized as follows:

1. Nineteen transition lines, including 13 thermal lines and 6 maser lines, were successfully detected toward our sample. The  $8_0 \rightarrow 7_1 A^+$  transition line at 95 GHz, one of the strongest class I  $\text{CH}_3\text{OH}$  maser lines, was detected in 52 sources, including 10 newly detected ones. For these 10 new maser sources, their line parameters were obtained by analysis of their spectral line data.
2. The line width of  $\text{CH}_3\text{OH}$  nonmasing emission lines was analyzed and we found the line width of higher- $J$  transitions tends to be larger than that of lower- $J$  transitions, which supports the fact that the inner HMSFRs have more violent turbulence or other motions than the outer regions. And the line width of all transition lines was found to increase with the bolometric luminosity, which agrees with the fact that the mass of the formed protostar should be related to the internal velocity dispersion of the dense clump.
3. Both sources with more detected  $\text{CH}_3\text{OH}$  thermal lines and sources with detections of  $\text{CH}_3\text{OH}$  masers tend to have higher gas column density, with respect to those with fewer  $\text{CH}_3\text{OH}$  thermal lines and nonmaser sources. In contrast, no significant difference can be found in  $T_{\text{dust}}$  and  $L_{\text{bol}}$  between them. This indicates that  $T_{\text{dust}}$  seems not to be important for the production of both thermal and maser lines of  $\text{CH}_3\text{OH}$ .
4. Through rotation diagram analysis of the detected thermal lines, we obtained the rotational temperature and  $N(\text{CH}_3\text{OH})$  for 111 sources. We found that  $A$ -type  $\text{CH}_3\text{OH}$  tends to have larger abundance than  $E$ -type  $\text{CH}_3\text{OH}$ , in the column density and the relative abundance  $\text{CH}_3\text{OH}/\text{H}_2$ . The column density ratio  $E/A$  of our sample is mostly less than 1.0 (about 70%), with a peak ratio of  $\sim 0.6$ , which is consistent with theoretical predictions, i.e., overabundance of  $A$ -type  $\text{CH}_3\text{OH}$  at low temperature leading to a low value of the  $E/A$  ratio. It is

also identical with the production mechanism of CH<sub>3</sub>OH, i.e., formation from successive hydrogenation of CO on cold dust surfaces.

- CH<sub>3</sub>OH abundance decreases beyond  $T_{\text{dust}} \sim 30$  K, which is basically consistent with theoretical results. Around 20–30 K, CH<sub>3</sub>OH ice photolysis could happen and lead to an enhancement of gas-phase CH<sub>3</sub>OH abundance via chemical desorption. However, at higher temperatures, recombination of dissociated CH<sub>3</sub>OH is less efficient than that at lower temperatures. In addition, a strong correlation between CH<sub>3</sub>OH and H<sub>2</sub> column density can be found, which implies CH<sub>3</sub>OH can be used as a reliable tracer of H<sub>2</sub>.

This work is supported by the National Key R&D Program of China (2022YFA1603102) and the Natural Science Foundation of China (NSFC; Nos. 12041302 and 11590782). We thank the operators and staff at the IRAM 30 m telescope for their assistance during our observations. J.J.Q. acknowledges support from the NSFC (Nos. 11973099 and 12003080), the Guangdong Basic and Applied Basic Research Foundation (No. 2019A1515110588), the Fundamental Research Funds for the Central Universities (Sun Yat-sen University, No. 22qntd3101), and science research grants from the China Manned Space Project with Nos. CMS-CSST-2021-A09 and CMS-CSST-2021-A10. Y.T.Y. is a member of the International Max Planck Research School (IMPRS) for Astronomy and Astrophysics at the Universities of Bonn and Cologne. Y. T.Y. and H.Z.Y. would like to thank the China Scholarship Council for its support.

### ORCID iDs

J. S. Zhang  <https://orcid.org/0000-0002-5161-8180>  
 Y. X. Wang  <https://orcid.org/0000-0001-9155-0777>  
 J. J. Qiu  <https://orcid.org/0000-0002-9829-8655>  
 Y. T. Yan  <https://orcid.org/0000-0001-5574-0549>  
 H. Z. Yu  <https://orcid.org/0000-0002-5634-131X>  
 J. L. Chen  <https://orcid.org/0000-0001-8980-9663>  
 Y. P. Zou  <https://orcid.org/0000-0002-5230-8010>

### References

Ball, J. A., Gottlieb, C. A., Lilley, A. E., & Radford, H. E. 1970, *ApJL*, **162**, L203  
 Batrla, W., Matthews, H. E., Menten, K. M., & Walmsley, C. M. 1987, *Natur*, **326**, 49  
 Beuther, H., Schilke, P., Sridharan, T. K., et al. 2002, *A&A*, **383**, 892  
 Bisschop, S. E., Jørgensen, J. K., van Dishoeck, E. F., & de Wachter, E. B. M. 2007, *A&A*, **465**, 913  
 Blake, G. A., Sutton, E. C., Masson, C. R., & Phillips, T. G. 1986, *ApJS*, **60**, 357  
 Blake, G. A., Sutton, E. C., Masson, C. R., & Phillips, T. G. 1987, *ApJ*, **315**, 621  
 Breen, S. L., Contreras, Y., Ellingsen, S. P., et al. 2018, *MNRAS*, **474**, 3898  
 Breen, S. L., Ellingsen, S. P., Caswell, J. L., et al. 2012a, *MNRAS*, **421**, 1703  
 Breen, S. L., Ellingsen, S. P., Caswell, J. L., et al. 2012b, *MNRAS*, **426**, 2189  
 Breen, S. L., Ellingsen, S. P., Caswell, J. L., et al. 2014, *MNRAS*, **438**, 3368  
 Breen, S. L., Ellingsen, S. P., Caswell, J. L., et al. 2016, *MNRAS*, **459**, 4066  
 Breen, S. L., Sobolev, A. M., Kaczmarek, J. F., et al. 2019, *ApJL*, **876**, L25  
 Brogan, C. L., Hunter, T. R., Townner, A. P. M., et al. 2019, *ApJL*, **881**, L39  
 Caswell, J. L., Fuller, G. A., Green, J. A., et al. 2010, *MNRAS*, **404**, 1029  
 Charnley, S. B., Tielens, A. G. G. M., & Rodgers, S. D. 1997, *ApJL*, **482**, L203  
 Chen, X., Ellingsen, S. P., Ren, Z.-Y., et al. 2019, *ApJ*, **877**, 90  
 Chen, X., Ellingsen, S. P., Shen, Z.-Q., Titmarsh, A., & Gan, C.-G. 2011, *ApJS*, **196**, 9  
 Chen, X., Gan, C.-G., Ellingsen, S. P., et al. 2013, *ApJS*, **206**, 9

Chen, X., Yang, T., Ellingsen, S. P., McCarthy, T. P., & Ren, Z.-Y. 2022, *ApJ*, **926**, 48  
 Cragg, D. M., Johns, K. P., Godfrey, P. D., & Brown, R. D. 1992, *MNRAS*, **259**, 203  
 Cragg, D. M., Sobolev, A. M., & Godfrey, P. D. 2005, *MNRAS*, **360**, 533  
 Cunningham, N., Fuller, G., & Avison, A. 2018, in IAU Symp. 336, *Astrophysical Masers: Unlocking the Mysteries of the Universe*, ed. A. Tarchi, M. J. Reid, & P. Castangia (Cambridge: Cambridge Univ. Press), 317  
 Cyganowski, C. J., Brogan, C. L., Hunter, T. R., & Churchwell, E. 2009, *ApJ*, **702**, 1615  
 Elia, D., Molinari, S., Schisano, E., et al. 2017, *MNRAS*, **471**, 100  
 Ellingsen, S. P. 2006, *ApJ*, **638**, 241  
 Feng, H., Wang, J., Li, S., et al. 2021, *PASJ*, **73**, 467  
 Fuchs, G. W., Cuppen, H. M., Ioppolo, S., et al. 2009, *A&A*, **505**, 629  
 Gerner, T., Beuther, H., Semenov, D., et al. 2014, *A&A*, **563**, A97  
 Goldsmith, P. F., & Langer, W. D. 1999, *ApJ*, **517**, 209  
 Gómez, L., Wyrowski, F., Pillai, T., Leurini, S., & Menten, K. M. 2011, *A&A*, **529**, A161  
 Guilloteau, S., & Lucas, R. 2000, in ASP Conf. Ser. 217, *Imaging at Radio through Submillimeter Wavelengths*, ed. J. G. Mangum & S. J. E. Radford (San Francisco, CA: ASP), 299  
 Guzmán, V. V., Goicoechea, J. R., Pety, J., et al. 2013, *A&A*, **560**, A73  
 Hatchell, J., Thompson, M. A., Millar, T. J., & MacDonald, G. H. 1998, *A&AS*, **133**, 29  
 He, J. H., Takahashi, S., & Chen, X. 2012, *ApJS*, **202**, 1  
 Herbst, E., & van Dishoeck, E. F. 2009, *ARA&A*, **47**, 427  
 Hunter, T. R., Brogan, C. L., Cyganowski, C. J., & Young, K. H. 2014, *ApJ*, **788**, 187  
 Jijina, J., Myers, P. C., & Adams, F. C. 1999, *ApJS*, **125**, 161  
 Jones, P. A., Burton, M. G., Cunningham, M. R., et al. 2008, *MNRAS*, **386**, 117  
 König, C., Urquhart, J. S., Csengeri, T., et al. 2017, *A&A*, **599**, A139  
 Kurtz, S., Hofner, P., & Álvarez, C. V. 2004, *ApJS*, **155**, 149  
 Ladd, E. F., Myers, P. C., & Goodman, A. A. 1994, *ApJ*, **433**, 117  
 Ladeyschikov, D. A., Bayandina, O. S., & Sobolev, A. M. 2019, *AJ*, **158**, 233  
 Leurini, S. 2005, PhD thesis, Rheinische Friedrich Wilhelms Univ. Bonn  
 Leurini, S., Menten, K. M., & Walmsley, C. M. 2016, *A&A*, **592**, A31  
 Leurini, S., Schilke, P., Menten, K. M., et al. 2004, *A&A*, **422**, 573  
 Levshakov, S. A., Kozlov, M. G., & Reimers, D. 2011, *ApJ*, **738**, 26  
 Linnartz, H., Ioppolo, S., & Fedoseev, G. 2015, arXiv:1507.02729  
 Liu, T., Evans, N. J., Kim, K.-T., et al. 2020, *MNRAS*, **496**, 2790  
 Lundquist, M. J., Kobulnicky, H. A., Kerton, C. R., & Arvidsson, K. 2015, *ApJ*, **806**, 40  
 Mangum, J. G., Darling, J., Henkel, C., & Menten, K. M. 2013, *ApJ*, **766**, 108  
 Mangum, J. G., & Wootten, A. 1993, *ApJS*, **89**, 123  
 Maud, L. T., Lumsden, S. L., Moore, T. J. T., et al. 2015, *MNRAS*, **452**, 637  
 McCarthy, T. P., Ellingsen, S. P., Voronkov, M. A., & Cimò, G. 2018, *MNRAS*, **477**, 507  
 Menten, K. M. 1991, *ApJL*, **380**, L75  
 Menten, K. M., Walmsley, C. M., Henkel, C., & Wilson, T. L. 1986, *A&A*, **157**, 318  
 Menten, K. M., Walmsley, C. M., Henkel, C., & Wilson, T. L. 1988, *A&A*, **198**, 253  
 Miao, D., Chen, X., Song, S.-M., et al. 2022, *ApJS*, **263**, 9  
 Minier, V., & Booth, R. S. 2002, *A&A*, **387**, 179  
 Molinari, S., Brand, J., Cesaroni, R., & Palla, F. 1996, *A&A*, **308**, 573  
 Müller, H. S. P., Schlöder, F., Stutzki, J., & Winnewisser, G. 2005, *JMoSt*, **742**, 215  
 Müller, H. S. P., Thorwirth, S., Roth, D. A., & Winnewisser, G. 2001, *A&A*, **370**, L49  
 Myers, P. C., Ladd, E. F., & Fuller, G. A. 1991, *ApJL*, **372**, L95  
 Nakano, M., & Yoshida, S. 1986, *PASJ*, **38**, 531  
 Pickett, H. M., Poynter, R. L., Cohen, E. A., et al. 1998, *JQSRT*, **60**, 883  
 Pihlström, Y. M., Sjouwerman, L. O., & Fish, V. L. 2011, *ApJL*, **739**, L21  
 Pihlström, Y. M., Sjouwerman, L. O., Frail, D. A., et al. 2014, *AJ*, **147**, 73  
 Purcell, C. R., Longmore, S. N., Burton, M. G., et al. 2009, *MNRAS*, **394**, 323  
 Reid, M. J., Menten, K. M., Brunthaler, A., et al. 2014, *ApJ*, **783**, 130  
 Reid, M. J., Menten, K. M., Brunthaler, A., et al. 2019, *ApJ*, **885**, 131  
 Ridge, N. A., Wilson, T. L., Megeath, S. T., Allen, L. E., & Myers, P. C. 2003, *AJ*, **126**, 286  
 Rivilla, V. M., Beltrán, M. T., Cesaroni, R., et al. 2017, *A&A*, **598**, A59  
 Rocha, W. R. M., Woitke, P., Pilling, S., et al. 2023, arXiv:2302.04239  
 Saito, H., Mizuno, N., Moriguchi, Y., et al. 2001, *PASJ*, **53**, 1037  
 Sobolev, A. M., Cragg, D. M., & Godfrey, P. D. 1997, *MNRAS*, **288**, L39  
 Song, S.-M., Chen, X., Shen, Z.-Q., et al. 2022, *ApJS*, **258**, 19  
 Sun, Y., Xu, Y., & Yang, J. 2012, *ChA&A*, **36**, 238

- Sutton, E. C., Blake, G. A., Masson, C. R., & Phillips, T. G. 1985, *ApJS*, **58**, 341
- Tang, X. D., Henkel, C., Wyrowski, F., et al. 2018, *A&A*, **611**, A6
- Townes, C. H., & Schawlow, A. L. 1955, *Microwave Spectroscopy* (New York: McGraw-Hill)
- Urquhart, J. S., Figura, C. C., Moore, T. J. T., et al. 2015, *MNRAS*, **452**, 4029
- Urquhart, J. S., König, C., Giannetti, A., et al. 2018, *MNRAS*, **473**, 1059
- Urquhart, J. S., Morgan, L. K., Figura, C. C., et al. 2011, *MNRAS*, **418**, 1689
- Urquhart, J. S., Wells, M. R. A., Pillai, T., et al. 2022, *MNRAS*, **510**, 3389
- van der Tak, F. F. S., van Dishoeck, E. F., & Caselli, P. 2000, *A&A*, **361**, 327
- van Gelder, M. L., Nazari, P., Tabone, B., et al. 2022, *A&A*, **662**, A67
- Voronkov, M. A., Caswell, J. L., Ellingsen, S. P., & Sobolev, A. M. 2010, *MNRAS*, **405**, 2471
- Wang, K., Wu, Y. F., Ran, L., Yu, W. T., & Miller, M. 2009, *A&A*, **507**, 369
- Watanabe, N., & Kouchi, A. 2002, *ApJL*, **571**, L173
- Watanabe, N., Nagaoka, A., Shiraki, T., & Kouchi, A. 2004, *ApJ*, **616**, 638
- Watanabe, N., Shiraki, T., & Kouchi, A. 2003, *ApJL*, **588**, L121
- Watanabe, Y., Nishimura, Y., Harada, N., et al. 2017, *ApJ*, **845**, 116
- Wirström, E. S., Geppert, W. D., Hjalmarsen, Å., et al. 2011, *A&A*, **533**, A24
- Woon, D. E. 2002, *ApJ*, **569**, 541
- Wouterloot, J. G. A., & Brand, J. 1989, *A&AS*, **80**, 149
- Wouterloot, J. G. A., Walmsley, C. M., & Henkel, C. 1988, *A&A*, **203**, 367
- Wu, Y., Zhang, Q., Yu, W., et al. 2006, *A&A*, **450**, 607
- Yan, Y. T., Zhang, J. S., Henkel, C., et al. 2019, *ApJ*, **877**, 154
- Yang, W., Xu, Y., Chen, X., et al. 2017, *ApJS*, **231**, 20
- Yang, W., Xu, Y., Choi, Y. K., et al. 2020, *ApJS*, **248**, 18
- Yang, K., Chen, X., Shen, Z.-Q., et al. 2017, *ApJ*, **846**, 160
- Yang, K., Chen, X., Shen, Z.-Q., et al. 2019, *ApJS*, **241**, 18